

Energy-Dependent Harmonic Ratios of the Cyclotron Features of X0331+53 in the 2004-2005 Outburst

M. Nakajima^{1,2}, T. Mihara² and K. Makishima^{2,3}

ABSTRACT

We report on changes of the cyclotron resonance energies of the recurrent transient pulsar, X0331+53 (V0332+53). The whole *RXTE* data acquired in the 2004-2005 outburst were utilized. The 3 – 80 keV source luminosity varied between 1.7×10^{36} and 3.5×10^{38} erg s⁻¹, assuming a distance of 7 kpc. We confirmed that the fundamental cyclotron resonance energy changed from ~ 22 to ~ 27 keV in a clear anti-correlation to the source luminosity, and without any hysteresis effects between the rising and declining phases of the outburst. In contrast, the second harmonic energy changed from ~ 49 to ~ 54 keV, implying a weaker fractional change as a function of the luminosity. As a result, the observed resonance energy ratio between the second harmonic and the fundamental was ~ 2.2 when the source was most luminous, whereas the ratio decreased to the nominal value of 2.0 at the least luminous state. Although the significance of this effect is model dependent, these results suggest that the fundamental and second harmonic resonances represent different heights in the accretion column, depending on the mass accretion rate.

Subject headings: pulsars: individual(X0331+53, 4U0115+63) — X-rays: binaries

¹School of Dentistry at Matsudo, Nihon University, 2-870-1, Sakae-cho Nishi, Matsudo-City, Chiba, JAPAN 271-8587

²Cosmic Radiation, The Institute of Physical and Chemical Research (RIKEN), 2-1 Hirosawa, Wako, Saitama, JAPAN 351-0198

³Department of Physics, University of Tokyo, 7-3-1 Hongo, Bunkyo-ku, Tokyo, JAPAN 113-0033

1. INTRODUCTION

Magnetic field strengths on the surface of accreting X-ray pulsars can be measured accurately by observing Cyclotron Resonant Scattering Feature (CRSF), because the fundamental electron cyclotron resonance energy E_{a1} is described as $E_{a1} = 11.6 B_{12}(1+z_g)^{-1}$ (keV). Here, B_{12} is the magnetic field strength in units of 10^{12} Gauss, and z_g is the gravitational redshift. Applying this relation to X-ray detected CRSFs, the magnetic field strengths of ~ 15 X-ray pulsars have been accurately measured (Trümper et al. 1978; White et al. 1983; Mihara 1995; Makishima et al. 1999; Coburn et al. 2002, and references therein). The results are clustered in a relatively narrow range of $(1 - 4) \times 10^{12}$ G (Makishima et al. 1999).

Since the cyclotron resonant scattering occurs near the pulsar surface, the resonance energies were believed to be constant and intrinsic to each pulsar. However, an unexpected CRSF energy change was found from the recurrent transient pulsar 4U 0115+63 with the *Ginga* observations performed in 1990 and 1991 (Mihara 1995; Mihara et al. 1998, 2004); in the 1991 minor outburst when the luminosity was $\sim \frac{1}{7}$ of that in the 1990 and other typical outbursts of this object, the value of E_{a1} was ~ 1.4 times higher than the so far reported $E_{a1} \sim 11$ keV. In order to interpret the change in E_{a1} , Mihara et al. (2004) proposed that the height of cyclotron scattering region in the accretion column changes depending on the X-ray luminosity. A further study of the luminosity-dependent CRSFs change was conducted by Nakajima (2006), Nakajima et al. (2006a,b), and Tsygankov et al. (2007), using *Rossi X-ray Timing Explorer (RXTE)* data of 4U 0115+63 acquired in 1999 and 2004. According to these results, E_{a1} increased from ~ 10 to ~ 16 keV as the source luminosity decreased across a narrow range of $(2 - 4) \times 10^{37}$ erg s $^{-1}$ (at an assumed distance of 7 kpc; Negueruela & Okazaki 2001). In addition, the second harmonics observed at ~ 20 keV disappeared as E_{a1} started to change.

This luminosity-dependent change in the CRSF energy has been found from another source, X0331+53 (V0332+53), with *Ginga*, *INTEGRAL* and *RXTE* observations (Mihara et al. 1998; Mowlavi et al. 2006; Nakajima 2006; Tsygankov et al. 2006, 2009). This source is a recurrent transient pulsar, and exhibits a very prominent fundamental CRSF at ~ 28 keV of the X-ray spectrum, as first discovered with *Ginga* (Makishima et al. 1990a) after a suggestion with *Temma* (Makishima et al. 1990b). Furthermore, its two higher harmonics have been discovered at energies of ~ 50 and ~ 75 keV (Coburn et al. 2005; Kreykenbohm et al. 2005; Pottschmidt et al. 2005). Thus, X0331+53 is the second object which has three or more CRSFs in the spectrum, following 4U 0115+63 (Santangelo et al. 1999; Heindl et al. 1999). However, compared with the results from 4U 0115+63, this object exhibited two intriguing differences (Mowlavi et al. 2006; Nakajima 2006; Tsygankov et al. 2006, 2009). One is that the change in E_{a1} started at a higher luminosity, 1×10^{38} erg s $^{-1}$,

at an assumed distance of 7 kpc (Negueruela et al. 1999). The other is that the second harmonic absorption feature persisted in the X-ray spectra through an outburst.

Including the above cases of 4U 0115+63 and X0331+53, the behavior of the fundamental CRSF has been extensively studied so far. In contrast, details of the second harmonic, including its possible luminosity dependence, are less understood, primarily because of lower data quality at higher energies. With this in mind, we analyzed the whole *RXTE* (ASM, PCA and HEXTE) data of X0331+53, acquired in a 2004-2005 outburst. As a result, we have discovered that the second CRSF energy E_{a2} possibly depends more weakly on the luminosity than E_{a1} . The E_{a2}/E_{a1} ratio was ~ 2.2 when the source was luminous, while it approached the nominal value of 2.0 toward lower luminosities. These results suggest that the two resonances take place at different heights in the same accretion columns, and that E_{a2} , formed at a lower height, provides a more reliable estimate of the surface field strength.

2. OBSERVATIONS and DATA REDUCTION

In order to study the luminosity-dependent changes of E_{a1} and E_{a2} of X0331+53, here we utilized all the *RXTE* data sets of this transient pulsar acquired in the 2004-2005 outburst. Figure 1a shows the whole light curve of this outburst acquired with the All Sky Monitor (ASM; Levine et al. 1996) onboard *RXTE*. An abrupt brightening was detected on 2004 November 25 (Swank et al. 2004), and the 2 – 12 keV flux continued to increase up to 1.1 Crab (Remillard 2004). As revealed by the ASM, the X-ray intensity declined toward middle of 2005 February, and exhibited a small recovery at the beginning of 2005 March, presumably synchronized with the 34.25 day orbital period (Zhang et al. 2005, and references therein). At the outburst peak, a number of target-of-opportunity observations were performed by *INTEGRAL*, *Swift*, and *RXTE*.

From 2004 November 27 through 2005 March 27, 108 pointing observations were made with the Proportional Counter Array (PCA; Jahoda et al. 2006) and the High Energy X-ray Timing Experiment (HEXTE; Rothschild et al. 1998) on board *RXTE*. Based on the inspection of the operation status of the five proportional counter units (PCU0~PCU4), we have selected the data sets acquired with PCU2, which worked throughout this outburst. As reported by Pottschmidt et al. (2005), HEXTE cluster A did not function from 2004 December 13 to 2005 January 14. Thus, we utilize only the data acquired with HEXTE cluster B.

Using part of the *RXTE* data sets that were acquired in the descent phase, the behavior of the fundamental CRSF was already studied (Mowlavi et al. 2006; Nakajima 2006;

Tsygankov et al. 2006). In the present paper, we complement these studies of the descent phase, by analyzing those datasets which were left unused. In addition, we analyze the ascent-phase datasets to examine whether the CRSF energy exhibits any hysteresis effects similar to those suggested by the 4U 0115+63 data (Nakajima et al. 2006a).

During the 4 months of observation, several energetic background events, such as large solar flares and precipitations of high-energy particles trapped in the radiation belts, affected some of the data sets. In order to exclude such low-quality data, we inspected the electron-rate light curves, and have selected 86 data sets with good quality as listed in Table 1. To analyze them, we utilized the HEASoft version 6.0.5. We assume 1% systematic error for all energy bins of the PCA data (same as in Nakajima et al. 2006a). All of the errors presented in this paper are 90% confidence levels.

3. DATA ANALYSIS AND RESULTS

3.1. Analysis of Representative Spectra

As shown in Figure 1, the intensity of X0331+53 changed largely in the ASM, PCA and HEXTE energy bands during this outburst. In addition, the hardness-ratio exhibited an anti-correlation to the source count rates as shown in Figure 1d. In order to investigate the luminosity related CRSFs changes through this outburst, we need to establish a unified spectral modeling which can be applied consistently to the data sets at all luminosity levels. So, we first examined pulse-phase-averaged PCA and HEXTE spectra from several representative data sets.

Since many of the data sets have rather short exposure, we selected four representative ones sets with relatively long exposures, denoted in Table 1 as Dec 2a, Dec 24, Jan 20, and Feb 13b; these represent the beginning, the peak, the declining phase, and the end of the outburst, respectively. Figure 2a shows the background-subtracted PCU2 (3 – 20 keV) and HEXTE B (20 – 80 keV) spectra obtained on these four occasions. The PCA background spectra were all estimated with the bright-background model (Jahoda et al. 2006), while the HEXTE backgrounds were extracted from the off-source position which is offset from the source by 1.5 degrees (Rothschild et al. 1998). The four spectra, even in their raw forms, clearly reveal the prominent fundamental CRSF at ~ 30 keV, which was observed in the previous (Makishima et al. 1990a,b) and the present (Kreykenbohm et al. 2005; Pottschmidt et al. 2005; Mowlavi et al. 2006; Nakajima 2006; Tsygankov et al. 2006, 2009) outburst of this object. Furthermore, the brighter two spectra clearly show the second harmonic resonance at ~ 60 keV.

From early days (e.g. White et al. 1983), continuum spectra of accretion powered pulsars were approximated by a power-law modified by exponential cutoff. In this paper, we employ NPEX (Negative and Positive power-law with EXponential) model (Mihara 1995; Makishima et al. 1999), which is described as

$$N(E) = (A_1 E^{-\alpha_1} + A_2 E^{+2.0}) \exp\left(-\frac{E}{kT}\right), \quad (1)$$

where E is the X-ray energy in units of keV, A_1 and α_1 are the normalization and photon index of the negative power-law, respectively, A_2 is the normalization of the positive power-law, and kT represents the cutoff-energy in units of keV. This model successfully reproduced the continuum spectra of 4U 0115+63 (Mihara et al. 2004; Nakajima 2006; Nakajima et al. 2006ab) at various luminosity levels. As already reported by several authors (e.g. Makishima et al. 1999; Coburn et al. 2002), the determinations of the cyclotron line parameters are affected by the continuum and the line modeling. Employing this model, we can compare the results of this work with the previous ones (Nakajima et al. 2006a). Therefore, we have selected this model.

We first attempted to fit the 4 spectra with the NPEX model, with A_1 , A_2 , α_1 , and kT all left free. Since the PCA background estimations are only good to a few percent, we further adjusted the background normalizations down to a level of $\sim 1\%$, following the method described in the *RXTE cook book*¹. However, as expected, the NPEX model gave acceptable fits to none of the four spectra. As revealed clearly by the data-to-model ratio in Figure 2b, all the four spectra exhibit the fundamental CRSF strongly at ~ 30 keV. The second harmonic CRSF is observed not only in the brighter two spectra, but also in the two fainter ones. In addition, the spectrum on Dec 24 exhibits evidence of the third harmonic CRSF at ~ 75 keV, as already reported by Coburn et al. (2005), Kreykenbohm et al. (2005), and Pottschmidt et al. (2005). Below, we concentrate on the fundamental and the second harmonic. The fluorescent Fe K_α lines at 6.4 keV with a width of $\sigma_{\text{Fe}} = 0.5$ keV are also taken into account (Pottschmidt et al. 2005; Nakajima 2006; Tsygankov et al. 2006).

In order to evaluate the fundamental and second CRSF parameters, we next introduce a cyclotron absorption model. Although some authors used Gaussian-shaped absorption cross section (Coburn et al. 2002; Kreykenbohm et al. 2004; Pottschmidt et al. 2005; Kreykenbohm et al. 2005; Mowlavi et al. 2006; Kretschmar et al. 2006; Klochkov et al. 2008) to reproduce the CRSF, we employ the cyclotron absorption (CYAB) factor which has been used successfully (Clark et al. 1990; Makishima et al. 1990a, 1999; Mihara 1995; Mihara et al. 1998; Nakajima 2006; Nakajima et al. 2006ab; Tsygankov et al. 2006, 2007,

¹See http://heasarc.gsfc.nasa.gov/docs/xte/recipes/cook_book.html

2009). The CYAB factor is described as

$$C_i(E) = \exp \left\{ -\frac{D_i (WE/E_{ai})^2}{(E - E_{ai})^2 + W_i^2} \right\} \quad (i = 1, 2), \quad (2)$$

where E_{ai} is the resonance energy, W_i is the resonance width, D_i is the resonance depth, and i is the harmonic number (with $i = 1$ fundamental). Using high-quality *Suzaku* data, Enoto et al. (2008) confirmed that eq.2 can successfully reproduce the 36 keV CRSF of the X-ray pulsar Her X-1, whereas the Gaussian-shaped absorption cross-section is less successful.

Since we already know that X0331+53 has the multiple CRSFs, we attempted to fit the data with an NPEX model multiplied by two CYAB factors (hereafter NPEX×CYAB2 model). The values of E_{a1} and E_{a2} were both left to vary independently, rather than constrained as $E_{a2} = 2E_{a1}$. As a result, the fits were much improved compared to the NPEX fit, as shown by the data-to-model ratios in Figure 2c. Due to the complex shape of the fundamental CRSFs, however, the NPEX×CYAB2 model is not yet fully successful, with $\chi^2_{\nu} \geq 1.2$. This fact was already reported from previous studies (Makishima et al. 1990a; Mihara 1995; Kreykenbohm et al. 2005; Pottschmidt et al. 2005).

In order to better describe the fundamental CRSF, Kreykenbohm et al. (2005) and Pottschmidt et al. (2005) introduced an additional Gaussian absorption (GABS) factor with a similar energy but a different width, thus constructing a nested double-Gaussian absorption profile. Therefore, let us try to explain away the fit residuals employing an additional GABS factor ², which is described as

$$G(E) = \exp \left[-\tau_{\text{ga}} \exp \left\{ -\frac{1}{2} \left(\frac{E - E_{\text{ga}}}{\sigma_{\text{ga}}} \right)^2 \right\} \right], \quad (3)$$

where E_{ga} is the line-center energy, σ_{ga} is the line width, and τ_{ga} is the optical depth at the line center. Although a more sophisticated CRSF modeling has been introduced by Schönherr et al. (2007), we employ the CYAB and GABS models in the present work, so that the results can be directly compared with previous studies of the luminosity dependence of CRSFs (Makishima et al. 1999; Mihara et al. 2004; Nakajima et al. 2006).

We fitted the four spectra by the NPEX×CYAB2×GABS model, namely the same NPEX×CYAB2 model but further multiplied by eq.3, in which the three GABS parameters (E_{ga} , σ_{ga} , τ_{ga}) were left free but E_{ga} was given an initial value close to E_{a1} . Due to low

²The original GABS model in XSPEC v11.3.2p had a bug related to the energy binnings as reported by Kitaguchi et al. (2007). In this paper, we utilized an updated version of GABS model with the bug fixed, provided by Keith Arnaud.

statistics in the higher energies, we fixed E_{a2} at $2E_{a1}$ in fitting the Dec 2a and Feb 13b data, while we left E_{a1} and E_{a2} both free and independent for the brighter two data sets. Then, as illustrated in Figure 2d, the four spectra have been described successfully with this model. The derived best-fit parameters are summarized in table 2. To see the configuration of the nested cyclotron models for the fundamental resonance, the spectrum observed on Dec 24 is presented in Figure 3 in its νF_ν form. Thus, the CYAB factor explains the gross shape of the fundamental CRSF, while the remaining narrow core is represented by the additional GABS factor. The value of E_{ga} agrees, within a few percent, with $E_{a1} \{1 + (W_1/E_{a1})^2\}$, or $\sim 1.2E_{a1}$ in the present case, where the CYAB factor becomes deepest (Mihara 1995; Makishima et al. 1999). For comparison, Kreykenbohm et al. (2005) and Pottschmidt et al. (2005) applied nested two GABS factors to the fundamental CRSF and obtained two Gaussian centroids which differs by 10 – 20%.

Since the continuum and the CRSF factor couple strongly, the 90%-confidence errors of individual fit parameters, given in Table 2, might be significantly underestimated. To examine this concern, we present in Figure 4 confidence contours between several pairs of the model parameters, obtained from the Dec 24 data. Thus, kT and the resonance energies are almost uncorrelated. Although the NPEX α_1 and the CYAB E_{a1} exhibit some correlations, the single-parameter 90% error ranges are confirmed to adequately represent the two-dimensional confidence ranges, without being under-estimated.

From these spectral analyses, we have established the unified model, which can reproduce the complex shape of the X0331+53 spectra regardless of the source luminosity. Hereafter, we use this model, namely, NPEX×CYAB2×GABS.

Although our analysis was performed with the HEAssoft version 6.0.5, the PCA response generator has been updated in the latest HEAssoft version 6.8, and a new PCA CALDB has been released on 2009 December 2. To examine possible effects of these software and calibration updates, we analyzed the Dec 24 data with the HEAssoft version 6.8 and the latest PCA CALDB. As a consequence, the cyclotron resonance energies changed only $\sim 1.0\%$, which is within statistical errors. Thus, we retain our results obtained with the HEAssoft version 6.0.5.

Just for comparison, we attempted to replace the CYAB modeling of the two CRSFs with that employing three GABS factors, with nested two for the fundamental and the other for the second harmonic. The three parameters of the three GABS factors were all left free. As a result, the model gave, for example, an acceptable fit ($\chi_\nu^2 \sim 1.16$) to the Dec 24 data. The obtained CRSF parameters are, $E_{1a} = 27.2_{-0.4}^{+0.8}$, $\sigma_{1a} = 8.10_{-1.05}^{+3.39}$, $\tau_{1a} = 1.46_{-0.28}^{+0.84}$, $E_{1b} = 25.6_{-0.3}^{+0.2}$, $\sigma_{1b} = 3.23_{-0.69}^{+0.77}$, $\tau_{1b} = 0.38_{-0.20}^{+0.49}$, $E_2 = 50.2_{-0.5}^{+0.7}$, $\sigma_2 = 7.08_{-0.85}^{+0.89}$, and $\tau_2 = 1.49_{-0.34}^{+0.34}$. Here, the subscript of 1a and 1b specify the parameters of the nested two GABS model for the

fundamental resonance. However, we retain our original modeling using the CYAB model, because it gives generally better fits: for example, the difference in χ^2 is 28 (for $\nu = 51$) in the case of the Dec 24 spectrum.

3.2. Analysis of the Date-sorted Spectra

We applied the model established in §3.1 to all the daily-averaged spectra, and studied the time evolution of the CRSF parameters. Since some data sets have insufficient statistics, the GABS model parameters did not converge. Following the obtained results in the previous subsection, we therefore fixed $E_{\text{ga}} = 1.2E_{a1}$ in all cases. The other procedures of the spectral analyses are the same as in §3.1.

As a result of this analysis, our model has given acceptable fits to all the data acquired in the major outburst spanning 2004 November through 2005 February. While the normalization parameters of the NPEX model varied in correlation with the luminosity, the NPEX kT , which is thought to give a measure of the electron temperature in the emission region (Makishima et al. 1999; Mihara et al. 2004), stayed rather constant like in the previous results on 4U 0115+63 (Nakajima et al. 2006a; Tsygankov et al. 2007). Although the fundamental CRSF parameters are well determined, the second CRSF parameters in some data sets became unconstrained due to insufficient data statistics in higher energies. In such cases, we fixed E_{a2} at $2E_{a1}$.

In contrast to the November-February outburst data, the remaining three data sets were observed in March during the minor outburst recovery (Figure 1). Since the source was rather faint on these occasions, the three spectra were reproduced with the NPEX model multiplied by a single CYAB factor describing the fundamental CRSF. Therefore, we do not discuss these data sets acquired in 2005 March.

Figure 5a shows the derived values of E_{a1} , together with 90%-confidence errors, as a function of the 3 – 80 keV source luminosity $L_{3,80}$. As already reported by Mowlavi et al. (2006), Nakajima (2006), and Tsygankov et al. (2006, 2009), E_{a1} thus changed from ~ 22 to ~ 27 keV as $L_{3,80}$ varied between 5.0×10^{37} and 3.5×10^{38} erg s $^{-1}$. When the data points in 5a are fitted by a linear function of $L_{3,80}$ having a form of

$$E_{a1} = E_{a1}^{(0)} \{1 + L_{3,80}/L_1\} \quad , \quad (4)$$

its two parameters (with 90% confidence errors) were obtained as $E_{a1}^{(0)} = 26.5 \pm 0.1$ keV and $L_1 = (-23.0 \pm 1.2) \times 10^{38}$ erg s $^{-1}$, with $\chi^2_\nu = 1.3$ ($\nu = 81$). In addition, we found no hysteresis effects in the variation of E_{a1} between the ascent and descent phases. This inference is consistent with a recent report by Tsygankov et al. (2009), who used the same data set.

Although the values of E_{a1} derived here are slightly discrepant with those measured from the same outburst by other authors (Kreykenbohm et al. 2005; Pottschmidt et al. 2005; Mowlavi et al. 2006; Tsygankov et al. 2006), the difference is within $\sim 10\%$, and can be attributed to the different modelings of the fundamental CRSF and the continuum.

As shown in Figure 5b, the second resonance energy E_{a2} , when determined independently, showed a considerably weaker dependence on $L_{3,80}$. When these data points are fitted by another linear function of $L_{3,80}$ as

$$E_{a2} = E_{a2}^{(0)} \{1 + L_{3,80}/L_2\} \quad , \quad (5)$$

we obtain $E_{a2}^{(0)} = 53.5 \pm 0.4$ keV and $L_2 = (-47.8 \pm 5.6) \times 10^{38}$ erg s $^{-1}$, together with $\chi_\nu^2 = 1.8$ ($\nu = 61$). Thus, $E_{a2}^{(0)}$ is consistent with $2.0E_{a1}^{(0)}$, while the luminosity dependence differs significantly between E_{a1} and E_{a2} (i.e., $|L_2| > |L_1|$ beyond their errors).

As a result of the above two correlations, the E_{a2}/E_{a1} ratio, shown in Figure 5c, increases from ~ 2.0 to ~ 2.2 as $L_{3,80}$ changes from 1.0×10^{38} erg s $^{-1}$ to 3.5×10^{38} erg s $^{-1}$. Since these ratios give $\chi_\nu^2 = 2.8$ ($\nu = 62$) when fitted with a constant value, they are inconsistent with being constant. In contrast, the fit became satisfactory with $\chi_\nu^2 = 1.2$ ($\nu = 61$), when we employ yet another linear function as

$$E_{a2}/E_{a1} = K \{1 + L_{3,80}/L_{21}\} \quad . \quad (6)$$

The two parameters were obtained as $K = 2.0 \pm 0.1$ and $L_{21} = (34 \pm 5) \times 10^{38}$ erg s $^{-1}$. Thus, the value of K is consistent with 2.0, while L_{21} remains finite. In other words, the E_{a2}/E_{a1} ratios exhibit a statistically significant dependence on the 3–80 keV luminosity. In §3.3 and §4.2, we discuss possible artifacts on these results introduced by our choice of the CRSF modeling.

3.3. Analysis of the Flux-sorted Spectra

In order to investigate the behavior of the second CRSF under better statistics, we next carried out the flux-sorted analysis which was already performed successfully on 4U 0115+63 (Nakajima 2006; Nakajima et al. 2006a,b). Specifically, we sorted the PCU2 and HEXTE cluster B data into 8 flux levels in reference to Figure 6, and co-added those data which fall in the same flux range. The flux was calculated every 64 sec, so that the flux sorting can catch up with short-term intrinsic variations, but not affected by photon-counting statistics. In addition, the whole data were divided into outburst ascent and descent phases (referring to Figure 6), to examine the CRSF energy changes for possible hysteresis effects. The procedure

of the spectral analysis is the same as in §3.2, but E_{ga} was left free, because of the improved statistics.

Figure 7a and 8a show the flux-sorted spectra of the ascent- and descent-phases, respectively. We again applied the NPEX×CYAB2×GABS model to these data, and found that the model gives acceptable fits as shown in Figure 7b and 8b.

As summarized in Table 3, this analysis allowed us to accurately determine the parameters of the fundamental and second CRSFs. Figure 9a and b show the values of E_{a1} and E_{a2} , respectively, against $L_{3,80}$. Thus, E_{a1} changed from ~ 22 to ~ 27 keV, while E_{a2} from ~ 49 to ~ 54 keV, thus reconfirming the essential features of Figure 5 with higher confidence. In fact, like in the case of the date-sorted spectra (§3.2), the fit with eq.4 to Figure 9a gave $E_{\text{a1}}^{(0)} = 27.4 \pm 0.6$ keV, $L_1 = (-16.5 \pm 3.3) \times 10^{38}$ erg s $^{-1}$, and $\chi_\nu^2 = 0.5$ ($\nu = 12$), while that with eq.5 to Figure 9b resulted in $E_{\text{a2}}^{(0)} = 53.3 \pm 0.5$ keV, $L_2 = (-45.7 \pm 7.0) \times 10^{38}$ erg s $^{-1}$, and $\chi_\nu^2 = 1.5$ ($\nu = 12$). The errors associated with these fit parameters are larger than those obtained in the date-sorted analysis, because here we left E_{ga} free while we previously fixed it at $1.2E_{\text{a1}}$. Figure 9c reconfirms that the resonance energy ratio $E_{\text{a2}}/E_{\text{a1}}$ changed from ~ 2.2 to the nominal value ~ 2.0 as the source luminosity decreased. The fit with eq.6 indicates $K = 2.0 \pm 0.1$, $L_{21} = (21.2 \pm 7.0) \times 10^{38}$ erg s $^{-1}$, and $\chi_\nu^2 = 0.3$ ($\nu = 12$).

Through the date-sorted and flux-sorted analyses, we confirmed that the luminosity-dependent changes in E_{a2} , E_{a1} and the $E_{\text{a2}}/E_{\text{a1}}$ ratio are statistically significant. Then, does this conclusion remain unaffected even if considering systematic errors? An immediate concern, namely spurious effects due to coupling between the continuum and CRSF parameters, can be ruled out because the error estimates are appropriate as indicated by Figure 4. Another problem is that the values of E_{a1} and E_{a2} do not pick up the deepest position of the CRSFs. Accordingly, we examined the behavior of the energy $\hat{E}_{\text{ai}} \equiv E_{\text{ai}} \{1 + (W_i/E_{\text{ai}})^2\}$ ($i = 1, 2$) at which the absorption is expected to become deepest (Mihara 1995). Figure 10 shows luminosity dependence of \hat{E}_{ai} . Thus, the values of \hat{E}_{ai} also exhibit a clear luminosity dependence. By fitting these data points with eq.4 and eq.5, we obtained the characteristic luminosities as $\hat{L}_1 = (-27.0 \pm 11.8) \times 10^{38}$ erg s $^{-1}$ and $\hat{L}_2 = (-44.3 \pm 8.0) \times 10^{38}$ erg s $^{-1}$. We hence reconfirm that the second resonance energy depends less steeply on the luminosity than the fundamental energy, although the difference between \hat{L}_1 and \hat{L}_2 is less significant than that between L_1 and L_2 , and the average $\hat{E}_{\text{a2}}/\hat{E}_{\text{a1}}$ ratio, 1.8–2.0 is smaller than 2.0 in contrast to the case of the $E_{\text{a2}}/E_{\text{a1}}$ ratios.

The largest systematic effect that may possibly affect the $E_{\text{a2}}/E_{\text{a1}}$ ratio would be the choice of the continuum and CRSF models. Since we have already tried in §3.1 replacing the CRSF model with the GABS model, here we examine the choice of the continuum. In order not to be affected by the CRSF modeling, we fitted the lowest-energy (3–13 keV)

and highest-energy (60–80 keV) ends of the flux-sorted fd1 and fd6 spectra, using a single NPEX continuum, and then normalized the overall spectrum to the best-fit model that was determined by each spectrum. The results, shown in Figure 11a, reveal the absorption features in a relatively model-free manner, with the continuum approximately removed. There, we have adjusted the energy scale and the ratio scale between the two spectra, so that the fundamental CRSFs best overlap. Thus, the fd1 ratio spectrum exhibits the 2nd harmonic at a significantly higher energy than the fd6 ratio. This result visualizes the luminosity-dependent change in the E_{a2}/E_{a1} ratio.

To examine the overall behavior of E_{a2} , E_{a1} , and their ratios under a different continuum model, we employed a power-law cutoff (PLCUT) model (Coburn et al. 2002), namely a power-law multiplied by an exponential cutoff factor. Figure 11b represents the same analysis as Figure 11a conducted with this continuum model. Thus, the result again visualizes that fd1 has a higher E_{a2}/E_{a1} ratio than fd6. We further fitted the fd1 and fd6 spectra by multiplying these PLCUT continua with the same absorption factors as used so far, and obtained the results summarized in Table 4. Thus, the fit goodness is comparable to those obtained with the NPEX continuum, and the values of E_{a1} and E_{a2} remain unchanged within errors, although the luminosity-dependent change in the E_{a2}/E_{a1} ratio became less significant.

As our further confirmation of the luminosity-dependent changes in the CRSF energies and their ratios, we fitted the fd1 and fd6 spectra simultaneously, with the NPEX×CYAB2 model. While the model parameters were generally allowed to differ between the two spectra, we imposed 4 stepwise constraints on the resonance energies. In the first step, we required E_{a1} to be the same between fd1 and fd6, and constrained E_{a2} to be twice E_{a1} . However, the fit was not acceptable, with $\chi^2/\nu = 2365/111$. Next, we allowed fd1 and fd6 to have different values of E_{a1} , but retained the 1:2 harmonic constraint on both spectra. This gave an improved fit with $\chi^2/\nu = 398/110$, implying that the two spectra have different resonance energies. Third, we allowed the two spectra to have different values of E_{a1} , but required them to have the same E_{a2}/E_{a1} ratio. The fit was then improved to $\chi^2/\nu = 321/110$, together with $E_{a2}/E_{a1} = 2.11 \pm 0.08$ which deviates from the nominal value 2.0. Finally, we left all the four resonance energies free, and obtained an improved fit with $\chi^2/\nu = 282/108$. This means that the E_{a2}/E_{a1} ratio is different not only from the harmonic condition, but also between the two spectra. (The fit is still unacceptable because we did not include the GABS factor to model the narrow core of the fundamental resonance.)

Finally, we repeated the same 4-step analyses, but using the PLCUT continuum. Then, the fit goodness from the 4 steps were $\chi^2/\nu = 2091/111$, $\chi^2/\nu = 1119/110$, $\chi^2/\nu = 341/110$, and $\chi^2/\nu = 254/108$. The implication is essentially the same as that derived with the NPEX continuum.

3.4. Additional Analyses

Since the flux-sorted spectra have rather good statistics, we examined them, up to 110 keV, for evidence of the third harmonic CRSF which was already reported by Kreykenbohm et al. (2005) and Pottschmidt et al. (2005). For this purpose, we further multiplied the NPEX×CYAB2×GABS model by an additional CYAB factor centered at ~ 75 keV, and applied it to the flux sorted spectra. Then, two data sets, fa1 and fd2, gave statistical significant (at $\sim 90\%$) evidence for the third CRSF, while the fundamental and second-harmonic CRSF parameters remained essentially the same as before. As a representative case, the third resonance parameters derived from the fa1 data are $E_{a3} = 73_{-2}^{+3}$ keV, $W_3 = 6_{-5}^{+7}$ keV, and $D_3 = 3_{-1}^{+23}$. These parameters are comparable to the previous results derived from the same *RXTE* data (Kreykenbohm et al. 2005; Pottschmidt et al. 2005). The third resonance energy was found to change no less than by $\sim \pm 3\%$, as the 3 – 80 keV luminosity varied from 3.16 to 3.59×10^{38} erg s $^{-1}$. Over this luminosity range, the E_{a3}/E_{a2} ratio stayed at an average value of 1.46 within a typical uncertainty of ± 0.05 . In contrast, the E_{a3}/E_{a1} ratio is systematically higher, 3.2. Therefore, E_{a3} and E_{a2} are consistent with being in the 2:3 harmonic ratio, while E_{a1} is inferred to be systematically lower, and depend significantly on the luminosity.

In addition to the investigation of the resonance energy changes, we examined whether the depths of the cyclotron resonance, D_i ($i = 1, 2$) and τ_{ga} , depend on the luminosity. Figure 12 shows these depth parameters, against the 3 – 80 keV luminosity. Both the fundamental and second CRSF depths, D_1 and D_2 respectively were found to decrease toward higher luminosities. Although τ_{ga} has large errors, it also exhibits the same tendency. These luminosity dependence in D_1 and D_2 are statistically significant, because fitting the D_1 and D_2 measurements with constant values gave reduced chi-square of 2.11 ($\nu = 13$), 5.88 ($\nu = 13$), respectively.

4. DISCUSSION

4.1. Modeling of the Spectra

We analyzed the whole set of *RXTE* PCA and HEXTE data of X0331+53, covering the 2004–2005 outburst, with two objectives in mind. One is to examine whether the luminosity-anticorrelated changes in the fundamental CRSF energy, observed during the outburst descent phase (Mowlavi et al. 2006; Nakajima 2006; Tsygankov et al. 2006), is also present during the outburst rising phase. This agrees with the conclusion of Tsygankov et al. (2009). The other is to examine the reported second harmonic resonance of this

pulsar (Coburn et al. 2005; Kreykenbohm et al. 2005; Pottschmidt et al. 2005) for possible luminosity-dependent changes, and compare the results with those of the fundamental CRSF.

Following our experience (e.g., Mihara 1995; Makishima et al. 1999), we adopted the NPEX model of eq.1 to represent the underlying 3–80 keV PCA and HEXTE continua, while two CYAB factors, eq.2, to account for the fundamental and second harmonic cyclotron features. Furthermore, to express the complex shape of the deep fundamental cyclotron feature as revealed in the previous studies (Makishima et al. 1990a; Kreykenbohm et al. 2005; Pottschmidt et al. 2005), we introduced a fine-tuning GABS factor, eq.3, which is nested with the fundamental CYAB factor. This NPEX×CYAB2×GABS model has given acceptable fits to all the daily-averaged and flux-sorted spectra. Furthermore, some of the spectra exhibited statistically significant evidence for the third harmonic resonance, as already reported by Coburn et al. (2005), Kreykenbohm et al. (2005), and Pottschmidt et al. (2005).

As exemplified in Figure 12 and Table 3, our fits generally imply that the fundamental and second harmonic resonances both have optical depths of 1.0–2.0, with comparable CYAB widths of ~ 8 keV. The fundamental CRSF is explained mainly by the CYAB model, with the additional GABS factor carrying $\sim 30\%$ of the optical depth when the source is luminous. Replacing the two CYAB models with two GABS models made the fits significantly worse (e.g. $\chi^2_\nu = 3.6$ in fa2 spectrum fitting), mainly because the observed flux falls considerably below the NPEX continuum, even at the 35 – 45 keV range which is in between the two cyclotron troughs (see Figure 3). This effect cannot be reproduced adequately by the GABS model which is symmetric between the red and blue sides, while it can be successfully accounted for by the CYAB factor of which the wing is more extended in the blue side due to the E^2 factor in eq.2.

4.2. Changes of the Cyclotron Resonance Energies

By applying the NPEX×CYAB2×GABS model to the daily-averaged and flux-sorted PCA+HEXTE spectra, we reconfirmed the reports by Mowlavi et al. (2006), Nakajima (2006), and Tsygankov et al. (2006, 2009), that the fundamental CRSF energy E_{a1} decreases as the source gets more luminous (Figure 9). Thus, X0331+53 becomes a second binary X-ray pulsar, after 4U 0115+63, of which E_{a1} correlates negatively with the source luminosity. Like the case of 4U 0115+63, this effect observed from X0331+53 can be explained by presuming that the cyclotron resonance “photosphere” gets higher in the accretion column, as the source luminosity increases and hence the column becomes taller (Basko & Sunyaev. 1976; Burnard et al. 1991; Mihara et al. 2004). These cases make a contrast to the behavior

of Her X-1, in which E_{a1} is reported to have been varying in a positive correlation with the luminosity (Gruber et al. 2001; Staubert et al. 2007), at least while the source is in a sub-Eddington regime. On the other hand, the recent works of Her X-1 (Staubert et al. 2007; Klochkov et al. 2008) reported that the anti-correlation behavior might exist when the source was in the super-Eddington regime.

In 4U 0115+63, the luminosity dependence of E_{a1} showed some hysteresis effects between the ascent and descent phases of the outburst (Nakajima et al. 2006). In contrast, we found, in agreement with Tsygankov et al. (2009), no such effects from X0331+53; in this source, the value of E_{a1} can be considered as a single-valued function of the source luminosity.

As the most important result of the present work, our NPEX×CYAB2×GABS modeling leads to an inference that the second resonance energy E_{a2} also correlates negatively with the source luminosity, but significantly more weakly than E_{a1} does. The two resonance energies decrease by $\Delta E_{a1}/E_{a1} \sim 12\%$ and $\Delta E_{a2}/E_{a2} \sim 5\%$, as the 3 – 80 keV luminosity increases from 1.0×10^{38} to 3.5×10^{38} erg s⁻¹. Consequently, the E_{a2}/E_{a1} ratio is consistent with the nominal value of 2.0 when the source is dim, while it increases to ~ 2.2 toward the outburst peak (Figure 9c). These effects are somewhat model dependent, and become less significant when the absorption profile and/or continuum shape are modeled in different ways. Although these effects were already noticed by Tsygankov et al. (2006), their spectra had rather low statistics in higher energies, and hence the second CRSF parameters were not well constrained.

While the relativistic effects (Araya & Harding. 1999) predicts the E_{a2}/E_{a1} ratios to be lower than the harmonic value of 2, actual measurements do not necessarily agree. The ratio exceeds 2.0 in some cases, and fall in the range 2.1 \sim 2.2; for example, 4U 1907+09 showed $E_{a1} \sim 18$ keV and $E_{a2} \sim 38$ keV (Cusumano et al. 1998); Vela X-1 showed $E_{a1} \sim 24$ keV and $E_{a2} \sim 52$ keV (Makishima et al. 1999; Kreykenbohm et al. 2002); and A0535+26 $E_{a1} \sim 50$ keV and $E_{a2} \sim 110$ keV (Kretschmar et al. 2006). In contrast, the ratios lower than 2.0 are reported in other cases, including the present *RXTE* data of X0331+53 themselves analyzed by some other authors (e.g., Pottschmidt et al. 2006) who generally took the deepest positions of the CRSFs as the resonance energies (§3.3).

A dominant origin of the reported scatter in the E_{a2}/E_{a1} ratio is presumably the use of different (e.g., CYAB vs. GABS) modeling of the CRSF profile. In this sense, our result of $E_{a2}/E_{a1} > 2$ is not free from this systematic problem. In fact, we find $E_{a2}/E_{a1} < 2$ if instead using $\hat{E}_{a2}/\hat{E}_{a1}$. Nevertheless, our result has some pieces of supporting evidence. One is that the CYAB modeling is more successful than that with the GABS factor (§3.1), when combined with the NPEX continuum. Another is that the third to second resonance energy ratio, E_{a3}/E_{a2} , is consistent with 1.5, while E_{a3}/E_{a1} is higher than the nominal value of 3.0.

Yet another support is provided by a physically self-consistent interpretation to be described in the next subsection. Even admitting that the absolute values of E_{a1} and E_{a2} might be subject to the systematic modeling uncertainty, the luminosity-dependent changes in the resonance energy ratio is considered to be robust as already shown in §3.3.

4.3. A Possible Explanation of the Observed Effect

Let us consider a possible explanation of the luminosity-dependent changes in E_{a1} , E_{a2} , and their ratios. According to Mihara et al. (2004) and Nakajima et al. (2006a), the observed changes in E_{a1} of 4U 0115+63 can be explained in terms of those in the height of cyclotron resonance “photosphere”, in combination with a dipole field geometry. In this scenario, the photosphere height above the neutron star surface, h_r , can be estimated as

$$\frac{h_r}{R_{\text{NS}}} \approx \left(\frac{E_{ai}}{E_{si}} \right)^{-1/3} - 1, \quad (7)$$

where R_{NS} is the neutron star radius, E_{si} is the resonance energy to be observed on the neutron-star surface, and i is the harmonic number.

Substituting the E_{a1} and E_{a2} values derived from the flux-sorted analysis (§3.3) into eq.7, h_r of the fundamental and second resonances have been estimated as shown in Figure 13. Here, we employed $E_{s1} = 27$ keV and $E_{s2} = 54$ keV, referring to the lowest-luminosity state in Figure 9. Also a typical value of $R_{\text{NS}} = 10$ km was employed. By translating the measurements into the photospheric heights, the figure thus yields two important implications. One is that the photosphere of the fundamental CRSF gets higher as the source luminosity increases, up to 800 m, or $\sim 8\%$ of R_{NS} . The other is that the second resonance photosphere, though increasing with the luminosity as well, is located closer to the surface than that of the fundamental, just reflecting the deviation of the E_{a2}/E_{a1} ratio from 2.0. The height difference between the two photospheres reach ~ 500 m when the source is most luminous. Like the estimation of h_r described above, we also calculated the resonance heights using the asymptotic energies \hat{E}_{si} which are derived from E_{ai} . Assume $\hat{E}_{s1} = 31.0$ keV and $\hat{E}_{s2} = 62.0$ keV, the luminosity-dependent height variations turned out to be ~ 500 m for \hat{E}_{a1} and ~ 400 m for \hat{E}_{a2} .

The altitude difference between the two photospheres can be explained qualitatively in the following manner. Theoretically (Harding & Daugherty. 1991; Araya & Harding. 1999, and references therein), the fundamental CRSF is predicted to have a cross section which is ~ 10 times larger than that of the second resonance. Then, we expect the fundamental photosphere to be formed nearly at the top of the accretion column. In contrast, the second

harmonic photosphere will appear at lower altitudes, where the column density integrated along our line of sight is expected to become higher. These effects have already predicted theoretically by Nishimura (2008). Then, a detailed modeling of the E_{a2}/E_{a1} ratio may provide a valuable probe into the density distribution along the accretion column, and its dependence on the mass accretion rate, although such a work is beyond the scope of the present paper.

Assuming that the luminosity-dependent changes in the resonance energies are caused by the photospheric height variations, and not, e.g., by relativistic effects (§4.2), the above physical picture further gives an *a posteriori* support to our finding of $E_{a2}/E_{a1} > 2.0$. In fact, if this ratio fell below 2.0 toward lower luminosities, we would have to conclude that the 2nd resonance photosphere is located higher than that of the fundamental, leading to a physically unrealistic condition.

4.4. Comparison with 4U 0115+63

Following our previous results on 4U 0115+63 (Mihara et al. 2004; Nakajima 2006; Nakajima et al. 2006a), the present work provides valuable information as to the luminosity dependent changes of the CRSF parameters in accreting X-ray pulsars. Although the fundamental CRSF of X0331+53 required the additional GABS factor (which was not needed in 4U 0115+63), the CYAB and GABS centroids varied similarly as shown in Figure 9 and 12. We therefore consider that this slight difference in the CRSF modeling does not hamper a direct comparison of the results from the two sources.

Let us first compare the luminosity dependence of E_{a1} in the two objects. As shown in Figure 14a, the resonance energy of X0331+53 depends on the luminosity much less steeply than that of 4U 0115+63, even though the sense of dependence is the same between them. Specifically, the dependence is expressed as $(\Delta E_{a1}/E_{a1})/(\Delta L_X/L_X) \sim 0.08$ in X0331+53, while $(\Delta E_{a1}/E_{a1})/(\Delta L_X/L_X) \sim 0.26$ in 4U 0115+63.

Assuming that the change in E_{a1} is caused by variations in the height of cyclotron resonance “photosphere”, the above difference suggests that the accretion column height of 4U 0115+63 responds more sensitively to changes in the mass accretion rate. This inference is reinforced by Figure 14b, which directly relates the estimated photosphere heights with the luminosity. This difference, in turn, may be attributed to differences in the accretion column shape. Indeed, as shown in Figure 15, the resonance depths D of X0331+53 depend negatively on the resonance width W/E_a , while the correlation is opposite in 4U 0115+63. According to previous studies (Isenberg et al. 1998; Kreykenbohm et al.

2004; Nakajima et al. 2006a, and references therein), this is considered to indicate that the accretion column in 4U 0115+63 has a tall cylindrical shape, whereas that in X0331+53 a flat coin-like shape.

The two sources are inferred to differ not only in the shape of the accretion column, but also in its area A_{col} . We expect the observed luminosity to be expressed as $L_X \cong A_{\text{col}} \sigma_{\text{SB}} T_{\text{eff}}^4$ (Bildsten et al. 1997), where σ_{SB} is the Stefan-Boltzmann constant, and T_{eff} is the accretion column temperature which can be approximated by the observed NPEX kT (Makishima et al. 1999; Mihara et al. 2004; Nakajima et al. 2006a). By substituting the derived parameters into this relation, we actually find X0331+53 to have a 1.43 times larger A_{col} than 4U 0115+63. The relatively shallow spin modulation in X0331+53 (Pottschmidt et al. 2005) supports this idea. Therefore, the accretion column in X0331+53 is considered to have a coin-like shape and a rather large area, so that its height depends only weakly on the mass accretion rate.

Let us finally discuss the behavior of the resonance depths. As already mentioned in the end of section 3.3, D_1 , D_2 , and τ_{ga} of X0331+53 have all been found to decrease toward higher luminosity. This change is in the same sense as those in 4U 0115+63 (Nakajima et al. 2006a) and GX301-2 (Okada et al. 2004). One possible mechanism causing such a dependence may be related to the appearance of higher harmonic resonances. As argued by several authors (Nakajima 2006; Nakajima et al. 2006a), an increased luminosity may give rise to significant higher harmonic resonances, which tend to make the fundamental resonance shallower through so-called “two-photon” effects (Alexander & Meszaros. 1991). In fact, the third CRSF of X0331+53 was confirmed to appear when the source becomes luminous.

In summary, we have quantified luminosity dependence of the fundamental and second resonance energies, and discovered clear luminosity-dependent changes in their ratio. In addition, we have discovered that the behavior of X0331+53 is qualitatively similar to that of 4U 0115+53, but differs quantitatively.

REFERENCES

- Alexander, S. G., & Meszaros, P. 1991, *ApJ*, 372, 565
- Araya, R. A., & Harding, A. K. 1999, *ApJ*, 517, 334
- Basko, M. M., & Sunyaev, R. A. 1976, *MNRAS*, 175, 395
- Bildsten, L., Chakrabarty, D., Chiu, J., Finger, M. H., Koh, D. T., Nelson, R. W., Prince,

- T. A., Rubin, B. C., Scott, D. M., Stollberg, M., Vaughan, B. A., Wilson, C. A., & Wilson, R. B. 1997, *ApJS*, 113, 367
- Burnard, D. J., Arons, J., & Klein, R. I. 1991, *ApJ*, 367, 575
- Clark, G., Woo, J., Nagase, F., Makishima, K., & Sakao, T. 1990, *ApJ*, 353, 274
- Coburn, W., Heindl, W. A., Rothschild, R. E., Gruber, D. E., Kreykenbohm, I., Wilms, J., Kretschmar, P., & Staubert, R. 2002, *ApJ*, 580, 394
- Coburn, W., Kretschmar, P., Kreykenbohm, I., McBride, V. A., Rothschild, R. E., & Wilms, J. 2005, *Atel*, 381
- Cusumano, G., di Salvo, T., Burderi, L., Orlandini, M., Piraino, S., Robba, N., & Santangelo, A. 1998, *A&A*, 338, L79
- Enoto, T., Makishima, K., Terada, Y., Mihara, T., Nakazawa, K., Ueda, T., Dotani, T., Kokubun, M., Nagase, F., Naik, S., Suzuki, M., Nakajima, M., & Takahashi, H. 2008, *PASJ*, 60, 57
- Gruber, D. E., Heindl, W. A., Rothschild, R. E., Coburn, W., Staubert, R., Kreykenbohm, I., & Wilms, J. 2001, *ApJ*, 562, 499
- Harding, A. K., Daugherty, J. K. 1991, *ApJ*, 374, 687
- Heindl, W. A., Coburn, W., Gruber, D. E., Pelling, M. R., Rothschild, R. E., Wilms, J., Pottschmidt, K., & Staubert, R. 1999, *ApJ*, 521, L49
- Isenberg, M., Lamb, D. Q., & Wang, J. C. L., 1998, *ApJ*, 505, 688
- Jahoda, K., Markwardt, C. B., Radeva, Y., Rots, A. H., Stark, M. J., Swank, J. H., Strohmayer, T. E., & Zhang, W., 2006, *ApJS*, 163, 401
- Kitaguchi, T., Enoto, T., Nakazawa, K., & Makishima, K., 2007, private communication
- Klochkov, D., Staubert, R., Postnov, K., Shakura, N., Santangelo, A., Tsygankov, S., Lutovinov, A., Kreykenbohm, I., & Wilms, J., 2008, *A&A*, 482, 907
- Kretschmar, P., Pottschmidt, K., Ferrigno, C., Kreykenbohm, I., Domingo, A., Wilms, J., Rothschild, R., Coburn, W., Kendziorra, E., Staubert, R., Schönherr, G., Santangelo, A., & Segreto, A., 2006, *Proceedings of the "The X-ray Universe 2005"*, 273
- Kreykenbohm, I., Coburn, W., Wilms, J., Kretschmar, P., Staubert, R., Heindl, W. A., & Rothschild, R. E. 2002, *A&A*, 395, 129

- Kreykenbohm, I., Wilms, J., Coburn, W., Kuster, M., Rothschild, R. E., Heindl, W. A., Kretschmar, P. & Staubert, R. 2004, *A&A*, 427, 975
- Kreykenbohm, I., Mowlavi, N., Produit, N., Soldi, S., Walter, R., Dubath, P., Lubinski, P., Trümper, M., Coburn, W., Santangelo, A., Rothschild, R. E., & Staubert, R. 2005, *A&A*, 433, 45
- Levine, A. M., Bradt, H., Cui, W., Jernigan, J. G., Morgan, E. H., Remillard, R., Shirey, R. E., & Smith, D. A., 1996, *ApJ*, 469, L33
- Makishima, K., Mihara, T., Ishida, M., Ohashi, T., Sakao, T., Tashiro, M., Tsuru, T., Kii, T., Makino, F., Murakami, T., Nagase, F., Tanaka, Y., Kunieda, H., Tawara, Y., Kitamoto, S., Miyamoto, S., Yoshida, A., & Turner, M. J. L. 1990a, *ApJ*, 365, 59
- Makishima, K., Ohashi, T., Kawai, N., Matsuoka, M., Koyama, K., Kunieda, H., Tawara, Y., Ushimaru, N., Corbet, R. H. D., Inoue, H., Kii, T., Makino, F., Mitsuda, K., Murakami, T., Nagase, F., Ogawara, Y., Tanaka, Y., Kitamoto, S., Miyamoto, S., Tsunemi, H., & Yamashita, K. 1990b, *PASJ*, 42, 295
- Makishima, K., Mihara, T., Nagase, F. & Tanaka, Y. 1999, *ApJ*, 525, 978
- Mihara, T., Ph.D. thesis in University of Tokyo 1995
- Mihara, T., Mihara, T., Makishima, K., & Nagase, F. 1998, *Adv. Space Res.* 22, 987
- Mihara, T., Makishima, K., & Nagase, F. 2004, *ApJ*, 610, 390
- Mowlavi, N., Kreykenbohm, I., Shaw, S. E., Pottschmidt, K., Wilms, J., Rodriguez, J., Produit, N., Soldi, S., Larsson, S., & Dubath, P. 2006, *A&A*, 451, 187
- Nakajima, M., Ph.D. thesis in Nihon University 2006
- Nakajima, M., Mihara, T., Makishima, K., & Niko, H. 2006a, *ApJ*, 646, 1125
- Nakajima, M., Mihara, T., Makishima, K., & Niko, H. 2006b, *Adv. Space Res.* 38, 2756
- Negueruela, I., Roche, P., Fabregat, J., & Coe, M. J. 1999, *MNRAS*, 307, 695
- Negueruela, I. & Okazaki, A. T. 2001, *A&A*, 369, 108
- Nishimura, O., 2008, *ApJ*, 672, 1127
- Okada, Y., Niko, H., Makishima, K., Nakajima, M., Mihara, T., Terada, Y., Nagase, F., & Tanaka, Y. 2004, *Proc. 5th INTEGRAL Workshop*

- Pottschmidt, K., Kreykenbohm, I., Wilms, J., Coburn, W., Rothschild, R. E., Kretschmar, P., McBride, V., Suchy, S., & Staubert, R. 2005, *ApJ*, 634, 97
- Remillard, R. 2004, *Atel*, 371
- Rothschild, R. E., Blanco, P. R., Gruber, D. E., Heindl, W. A., MacDonald, D. R., Marsden, D. C., Pelling, M. R., Wayne, L. R., & Hink, P. L. 1998, *ApJ*, 496, 538
- Santangelo, A., Segreto, A., Giarrusso, S., dal Fiume, D., Orlandini, M., Parmar, A. N., Oosterbroek, T., Bulik, T., Mihara, T., Campana, S., Israel, G. L., & Stella, L. 1999, *ApJ*, 523, L85
- Schönherr, G., Wilms, J., Kretschmar, P., Kreykenbohm, I., Santangelo, A., Rothschild, R. E., Coburn, W., Staubert, R. 2007, *A&A*, 472, 353
- Staubert, R., Shakura, N. I., Postnov, K., Wilms, J., Rothschild, R. E., Coburn, W., Rodina, L., & Klochkov, D. 2007, *A&A*, 465, L25
- Swank, J., Remillard, R., & Smith, E. 2004, *Atel*, 349
- Trümper, J., Pietsch, W., Reppin, C., Voges, W., Staubert, R., & Kendziorra, E. 1978, *ApJ*, 219, L105
- Tsygankov, S. S., Lutovinov, A. A., Churazov, E. M., & Sunyaev, R. A., 2006, *MNRAS*, 371, 19
- Tsygankov, S. S., Lutovinov, A. A., & Serber, A., 2009, *astro-ph/0909.5379*
- Tsygankov, S. S., Lutovinov, A. A., Churazov, E. M., & Sunyaev, R. A., 2007, *AstL*, 33, 368
- White, N., Swank, J., & Holt, S.S. 1983, *ApJ*, 270, 711
- Zhang, S., Qu, J. L., Song, L. M., & Torres, D. F. 2005, *ApJ*, 630, 65

Table 1. The log of *RXTE* observations of X0331+53 in the 2004–2005 outburst.

Date (2004/2005)	Start/End Time ^a (UT)	PCA Rate ^b [c s ⁻¹]	HEXTE Rate ^c [c s ⁻¹]	Date (2004/2005)	Start/End Time ^a (UT)	PCA Rate ^b [c s ⁻¹]	HEXTE Rate ^c [c s ⁻¹]
Nov 27	14:06/14:13	541 ± 2	35.9 ± 1.4	Jan 11d	14:48/15:52	2049 ± 4	73.3 ± 0.4
Dec 1	06:54/07:41	848 ± 2	44.5 ± 0.4	Jan 14	08:43/15:59	1841 ± 4	66.8 ± 0.2
Dec 2a	03:20/04:12	973 ± 2	49.9 ± 0.4	Jan 15a	00:28/04:33	1789 ± 4	64.9 ± 0.2
Dec 2b	19:16/20:11	1042 ± 2	52.2 ± 0.4	Jan 15b	08:19/15:14	1770 ± 3	64.4 ± 0.2
Dec 3	18:52/00:25	1121 ± 2	54.1 ± 0.2	Jan 15c	20:57/21:17	1708 ± 4	61.7 ± 0.5
Dec 4a	01:00/01:30	1100 ± 2	52.1 ± 0.5	Jan 15d	22:28/03:59	1707 ± 3	61.3 ± 0.2
Dec 4b	02:34/03:14	1141 ± 2	55.2 ± 0.4	Jan 16a	09:30/14:29	1623 ± 3	60.7 ± 0.2
Dec 4c	05:52/06:25	1155 ± 2	54.3 ± 0.6	Jan 16b	20:33/02:12	1604 ± 3	59.5 ± 0.2
Dec 4d	09:15/09:39	1189 ± 2	57.2 ± 0.5	Jan 17a	02:49/03:36	1578 ± 3	59.2 ± 0.4
Dec 4e	12:00/18:02	1176 ± 2	56.6 ± 0.2	Jan 17b	07:31/13:00	1541 ± 3	58.1 ± 0.2
Dec 4f	18:21/00:00	1204 ± 2	56.3 ± 0.2	Jan 17c	20:10/00:13	1508 ± 3	56.8 ± 0.2
Dec 5a	00:36/01:08	1219 ± 2	56.4 ± 0.5	Jan 18a	00:50/01:55	1475 ± 3	56.1 ± 0.3
Dec 5b	13:11/14:16	1287 ± 3	60.0 ± 0.4	Jan 18b	07:08/12:58	1316 ± 3	56.0 ± 0.2
Dec 5c	17:55/19:15	1328 ± 3	60.7 ± 0.5	Jan 18c	21:17/01:24	1433 ± 3	54.8 ± 0.2
Dec 6	17:36/18:51	1443 ± 3	65.7 ± 0.5	Jan 19a	02:01/02:46	1440 ± 3	55.0 ± 0.4
Dec 7	17:05/17:51	1545 ± 3	69.7 ± 0.5	Jan 19b	03:39/08:41	1424 ± 3	54.0 ± 0.2
Dec 13	18:30/19:11	2392 ± 5	88.9 ± 0.6	Jan 20	07:53/11:30	1366 ± 3	54.9 ± 0.2
Dec 14	17:25/18:21	2557 ± 5	93.7 ± 0.4	Jan 21	07:42/08:21	1295 ± 3	53.1 ± 0.4
Dec 15a	12:18/14:20	2609 ± 5	95.7 ± 0.3	Jan 23	05:07/06:32	1201 ± 2	50.3 ± 0.3
Dec 15b	14:51/19:42	2614 ± 5	96.9 ± 0.2	Jan 24a	06:23/13:49	1183 ± 2	49.5 ± 0.2
Dec 15c	20:36/21:17	2604 ± 5	95.4 ± 0.5	Jan 24b	14:13/15:07	1165 ± 2	48.9 ± 0.4
Dec 16	02:26/03:02	2665 ± 5	96.2 ± 0.5	Jan 25	07:26/10:36	1099 ± 2	48.4 ± 0.2
Dec 17	11:44/12:51	2789 ± 6	97.2 ± 0.4	Jan 28	10:57/11:43	943 ± 2	43.7 ± 0.4
Dec 18	01:41/02:53	2851 ± 6	100.5 ± 0.5	Jan 29	14:25/14:51	927 ± 2	43.9 ± 0.6
Dec 19a	14:14/15:10	2870 ± 6	100.9 ± 0.4	Jan 31	08:48/09:13	858 ± 2	41.8 ± 0.5
Dec 19b	20:08/20:32	2859 ± 6	98.1 ± 0.7	Feb 2	08:09/08:23	780 ± 2	37.8 ± 0.7
Dec 20	23:58/00:58	3017 ± 6	105.4 ± 0.5	Feb 4	05:39/05:54	780 ± 2	38.5 ± 0.6
Dec 22	02:49/03:32	3023 ± 6	103.9 ± 0.7	Feb 6a	13:34/16:19	681 ± 1	35.2 ± 0.2
Dec 24	09:20/16:11	3163 ± 6	101.7 ± 0.2	Feb 6b	18:16/18:45	696 ± 1	35.8 ± 0.4
Dec 25	08:32/15:48	3120 ± 6	100.0 ± 0.1	Feb 6c	23:00/23:36	665 ± 1	35.7 ± 0.4
Dec 28	05:28/06:21	3119 ± 6	99.0 ± 0.5	Feb 8	06:46/07:34	618 ± 1	32.9 ± 0.3
Dec 29a	05:52/06:30	3078 ± 6	99.5 ± 0.4	Feb 9	18:02/18:14	545 ± 2	30.8 ± 1.0
Dec 29b	21:52/22:29	3098 ± 6	102.4 ± 0.6	Feb 10	14:52/15:26	516 ± 1	29.6 ± 0.5
Dec 30	13:35/14:20	3040 ± 6	97.7 ± 0.5	Feb 12a	01:23/04:10	478 ± 1	24.2 ± 1.1
Jan 6a	06:23/06:38	2582 ± 5	85.5 ± 0.8	Feb 12b	17:04/21:06	446 ± 1	24.4 ± 0.3
Jan 6b	15:15/16:04	2626 ± 5	87.4 ± 0.4	Feb 13a	00:58/01:45	440 ± 1	25.6 ± 0.6
Jan 8a	10:11/10:34	2475 ± 5	79.0 ± 0.6	Feb 13b	04:12/08:18	427 ± 1	25.9 ± 0.2
Jan 8b	14:25/14:56	2490 ± 5	83.7 ± 0.6	Feb 13c	11:45/14:10	401 ± 1	24.4 ± 0.2
Jan 8c	17:41/18:25	2445 ± 5	83.3 ± 0.5	Feb 13d	18:01/19:01	390 ± 1	23.6 ± 0.3
Jan 10	10:57/16:02	2157 ± 4	76.5 ± 0.2	Feb 15	12:07/14:56	329 ± 1	21.0 ± 0.3
Jan 11a	01:01/01:24	2112 ± 4	72.7 ± 0.5	Mar 7	07:07/08:06	33.8 ± 0.1	2.6 ± 0.2
Jan 11b	08:20/09:18	2159 ± 4	74.2 ± 0.4	Mar 9	07:54/08:10	75.9 ± 0.5	5.1 ± 0.7
Jan 11c	11:32/12:32	2106 ± 4	74.0 ± 0.4	Mar 18	01:34/01:50	12.4 ± 0.2	0.8 ± 0.4

^aStart and end time (UT) of the PCA observations.

^bBackground subtracted count rates of PCU2 in the 3-20 keV energy range.

^cBackground subtracted count rates of HEXTE cluster B in the 20-80 keV energy range.

Table 2. The best-fit parameters of NPEX×CYAB2×GABS model, determined by the four representative spectra shown in Figure 2.

parameters	Obs. Date			
	Dec 2a	Dec 24	Jan 20	Feb 13b
I_{iron}^a	1.54 ± 0.26	$6.64^{+1.03}_{-0.99}$	$2.59^{+0.36}_{-0.35}$	$0.65^{+0.11}_{-0.08}$
α_1	-0.22 ± 0.07	$-0.22^{+0.13}_{-0.10}$	$-0.30^{+0.10}_{-0.08}$	$0.07^{+0.09}_{-0.08}$
kT (keV)	$6.25^{+2.82}_{-1.18}$	$5.62^{+0.17}_{-0.16}$	$5.57^{+0.90}_{-0.79}$	$6.16^{+0.78}_{-0.61}$
E_{a1} (keV)	$25.8^{+0.6}_{-1.2}$	$21.1^{+1.0}_{-2.1}$	$24.4^{+0.9}_{-1.5}$	$25.4^{+1.0}_{-1.2}$
W_1 (keV)	$8.69^{+1.60}_{-1.86}$	$10.71^{+2.96}_{-1.67}$	$8.61^{+2.00}_{-1.44}$	$9.83^{+1.11}_{-1.52}$
D_1	$1.32^{+0.27}_{-0.29}$	$1.10^{+0.11}_{-0.19}$	$1.14^{+0.24}_{-0.36}$	$1.05^{+0.35}_{-0.27}$
E_{a2} (keV)	51.7 (fixed)	49.5 ± 0.3	$51.5^{+1.3}_{-1.6}$	50.8 (fixed)
W_2 (keV)	$7.78^{+6.19}_{-3.04}$	$4.86^{+1.17}_{-1.07}$	$5.60^{+6.22}_{-4.60}$	9.83(fixed)
D_2	$1.77^{+0.75}_{-0.90}$	1.35 ± 0.12	$1.95^{+6.99}_{-0.61}$	$1.90^{+0.47}_{-0.30}$
E_{ga} (keV)	$29.8^{+1.0}_{-0.7}$	26.4 ± 0.3	$29.3^{+0.5}_{-0.4}$	$29.7^{+0.5}_{-0.3}$
σ_{ga} (keV)	$2.41^{+0.73}_{-1.35}$	$3.14^{+0.63}_{-0.57}$	$2.70^{+0.72}_{-0.91}$	$2.42^{+0.56}_{-0.43}$
τ_{ga}	$0.90^{+0.55}_{-0.63}$	$0.48^{+0.34}_{-0.20}$	$0.92^{+0.58}_{-0.46}$	$1.33^{+0.46}_{-0.47}$
L_X^b	1.37	3.65	1.76	0.65
$\chi^2_\nu(\nu)$	0.77(52)	0.55(51)	0.66(51)	0.67(52)

^aIn units of 10^{-2} photons $\text{cm}^{-1} \text{s}^{-1}$.

^bIn units of $\times 10^{38}$ ergs s^{-1} in 3 – 80 keV.

Table 3. The best-fit NPEX×CYAB2×GABS model parameters, determined by the flux-sorted spectra.

flux level	NPEX		CYAB					GABS			L_X^a	χ_ν^2	
	α_1	kT (keV)	E_{a1} (keV)	W_1 (keV)	D_1	E_{a2} (keV)	W_2 (keV)	D_2	E_{ga} (keV)	σ_{ga} (keV)			τ_{ga}
ascent phase													
fa1	$-0.23^{+0.13}_{-0.11}$	$5.43^{+0.14}_{-0.12}$	$20.9^{+1.1}_{-2.0}$	$10.79^{+2.68}_{-1.83}$	$0.99^{+0.13}_{-0.16}$	49.3 ± 0.3	$4.33^{+0.88}_{-0.86}$	$1.22^{+0.10}_{-0.09}$	$26.4^{+0.4}_{-0.3}$	$3.39^{+0.46}_{-0.48}$	$0.55^{+0.27}_{-0.21}$	3.59	0.81
fa2	$-0.24^{+0.12}_{-0.10}$	$5.46^{+0.17}_{-0.15}$	$22.2^{+1.1}_{-1.9}$	$10.08^{+2.92}_{-1.85}$	$1.02^{+0.20}_{-0.21}$	49.5 ± 0.3	$4.40^{+1.18}_{-1.10}$	$1.43^{+0.15}_{-0.12}$	$27.4^{+0.5}_{-0.3}$	$3.47^{+0.49}_{-0.56}$	$0.68^{+0.34}_{-0.29}$	3.26	0.59
fa3	$-0.25^{+0.12}_{-0.09}$	$6.03^{+0.50}_{-0.39}$	$23.0^{+1.0}_{-2.2}$	$10.21^{+3.62}_{-1.93}$	$1.22^{+0.22}_{-0.29}$	$50.3^{+0.5}_{-0.6}$	$6.05^{+2.59}_{-2.08}$	$1.99^{+0.29}_{-0.27}$	$27.6^{+0.5}_{-0.3}$	$3.17^{+0.78}_{-0.83}$	$0.67^{+0.54}_{-0.36}$	3.07	0.71
fa5	$-0.24^{+0.13}_{-0.10}$	$5.58^{+0.71}_{-0.50}$	$23.5^{+1.2}_{-2.0}$	$9.83^{+2.64}_{-2.00}$	$0.96^{+0.24}_{-0.31}$	$51.1^{+1.1}_{-1.0}$	$5.35^{+4.55}_{-3.27}$	$1.63^{+0.62}_{-0.41}$	$29.1^{+0.4}_{-0.3}$	$3.23^{+0.59}_{-0.58}$	$1.03^{+0.47}_{-0.36}$	1.79	0.57
fa6	$-0.20^{+0.10}_{-0.09}$	$5.60^{+0.25}_{-0.23}$	$24.3^{+0.7}_{-1.1}$	$9.37^{+1.74}_{-1.29}$	$1.04^{+0.18}_{-0.16}$	51.1 ± 0.4	$4.53^{+1.47}_{-1.29}$	$1.88^{+0.31}_{-0.23}$	$29.3^{+0.3}_{-0.2}$	$2.93^{+0.34}_{-0.41}$	0.98 ± 0.27	1.53	0.55
fa7	$-0.25^{+0.11}_{-0.06}$	$6.52^{+5.14}_{-1.36}$	$26.5^{+1.0}_{-1.8}$	$6.84^{+1.79}_{-1.93}$	$1.52^{+0.33}_{-0.44}$	$51.8^{+8.1}_{-2.9}$	$5.75^{+6.22}_{-4.75}$	$3.63^{+60.76}_{-2.21}$	$31.3^{+1.1}_{-1.3}$	$0.91^{+0.60}_{-0.42}$	9.15(fixed)	1.10	0.64
descent phase													
fd1	$-0.29^{+0.13}_{-0.10}$	$5.56^{+0.51}_{-0.36}$	$21.6^{+1.2}_{-4.3}$	$10.00^{+5.88}_{-2.04}$	$1.03^{+0.20}_{-0.37}$	49.3 ± 0.9	$6.11^{+3.70}_{-2.95}$	$1.09^{+0.30}_{-0.25}$	$26.5^{+0.7}_{-0.6}$	$3.32^{+0.95}_{-0.95}$	$0.50^{+0.60}_{-0.30}$	3.54	0.64
fd2	$-0.29^{+0.12}_{-0.09}$	$5.52^{+1.84}_{-0.72}$	$22.9^{+1.0}_{-2.7}$	$8.30^{+5.70}_{-1.91}$	$1.12^{+0.37}_{-0.56}$	$49.7^{+1.6}_{-1.7}$	$8.61^{+8.08}_{-7.19}$	$1.23^{+1.23}_{-0.57}$	$27.8^{+1.1}_{-1.0}$	$3.38^{+1.07}_{-1.57}$	$0.61^{+0.59}_{-0.50}$	3.16	0.53
fd3	$-0.24^{+0.10}_{-0.09}$	$5.09^{+0.32}_{-0.28}$	$22.9^{+0.8}_{-1.1}$	$8.37^{+1.43}_{-1.25}$	$0.99^{+0.21}_{-0.25}$	$50.3^{+0.7}_{-0.8}$	$3.40^{+2.39}_{-2.40}$	$1.61^{+2.30}_{-0.34}$	$28.3^{+0.4}_{-0.3}$	$2.92^{+0.45}_{-0.51}$	$0.81^{+0.33}_{-0.28}$	2.72	0.80
fd4	$-0.26^{+0.10}_{-0.08}$	$5.37^{+0.32}_{-0.27}$	$23.9^{+0.7}_{-0.9}$	$9.03^{+1.48}_{-1.28}$	$1.18^{+0.18}_{-0.17}$	51.7 ± 0.5	$4.94^{+1.79}_{-1.68}$	$1.86^{+0.23}_{-0.23}$	$28.6^{+0.3}_{-0.2}$	$2.77^{+0.38}_{-0.51}$	0.73 ± 0.26	2.23	0.61
fd5	$-0.26^{+0.11}_{-0.08}$	$5.31^{+0.23}_{-0.25}$	$23.7^{+0.6}_{-1.0}$	$9.23^{+0.6}_{-1.05}$	$1.01^{+0.16}_{-0.14}$	$51.6^{+0.4}_{-0.5}$	$4.56^{+1.33}_{-1.52}$	$1.88^{+0.22}_{-0.22}$	28.9 ± 0.2	2.94 ± 0.28	$0.95^{+0.23}_{-0.19}$	1.87	0.68
fd6	$-0.31^{+0.07}_{-0.06}$	$6.28^{+1.04}_{-0.55}$	$25.2^{+0.6}_{-0.8}$	$8.99^{+1.47}_{-1.01}$	$1.35^{+0.19}_{-0.18}$	$52.4^{+1.0}_{-0.7}$	$7.95^{+3.62}_{-2.29}$	$2.28^{+0.56}_{-0.41}$	29.3 ± 0.3	$2.27^{+0.55}_{-0.74}$	$0.89^{+0.39}_{-0.40}$	1.45	0.44
fd7	$-0.04^{+0.09}_{-0.10}$	$5.54^{+0.70}_{-0.37}$	$25.7^{+0.5}_{-0.9}$	$7.58^{+1.52}_{-0.97}$	$1.16^{+0.22}_{-0.26}$	$51.8^{+1.0}_{-0.7}$	$5.74^{+3.62}_{-2.32}$	$1.96^{+0.44}_{-0.37}$	$30.1^{+0.3}_{-0.4}$	$2.56^{+0.55}_{-0.58}$	$0.97^{+0.45}_{-0.34}$	0.79	1.08
fd8	$0.07^{+0.09}_{-0.06}$	$7.24^{+8.88}_{-1.22}$	$26.8^{+0.5}_{-0.9}$	$10.03^{+2.01}_{-1.46}$	$1.77^{+0.36}_{-0.30}$	$54.4^{+4.1}_{-2.0}$	$8.24^{+9.40}_{-5.15}$	$4.09^{+5.84}_{-1.34}$	29.2 ± 0.7	$1.38^{+1.12}_{-0.97}$	$1.24^{+1.81}_{-0.93}$	0.56	0.42

^a $\times 10^{38}$ ergs s⁻¹ in 3 – 80 keV

Table 4. The best-fit PLCUT×CYAB2×GABS model parameters, determined by the flux-sorted spectra.

flux level	PLCUT			CYAB						GABS			L_X^a	χ_ν^2
	Γ	E_{cut} (keV)	E_{fold} (keV)	E_{a1} (keV)	W_1 (keV)	D_1	E_{a2} (keV)	W_2 (keV)	D_2	E_{ga} (keV)	σ_{ga} (keV)	τ_{ga}		
fd1	$-0.34^{+0.09}_{-0.07}$	$2.24^{+1.24}_{-1.24}$	$7.19^{+0.73}_{-0.53}$	$22.5^{+0.6}_{-3.1}$	$7.75^{+8.59}_{-1.03}$	$1.03^{+0.17}_{-0.70}$	$49.8^{+0.9}_{-0.9}$	$7.68^{+4.10}_{-2.79}$	$1.17^{+10.61}_{-3.71}$	$27.24^{+0.78}_{-1.97}$	$3.20^{+1.47}_{-1.01}$	$0.40^{+1.08}_{-0.24}$	35.42	0.74
fd6	$-0.26^{+0.14}_{-0.07}$	$1.69^{+1.95}_{-0.69}$	$10.16^{+2.13}_{-0.80}$	$25.3^{+0.5}_{-1.0}$	$8.44^{+1.22}_{-0.69}$	$1.38^{+0.17}_{-0.22}$	$53.5^{+1.0}_{-0.8}$	$12.64^{+3.76}_{-2.10}$	$2.96^{+13.44}_{-7.58}$	$29.55^{+0.32}_{-0.32}$	$2.33^{+0.63}_{-0.76}$	$0.87^{+0.50}_{-0.39}$	14.50	0.61

^a $\times 10^{38}$ ergs s⁻¹ in 3 – 80 keV

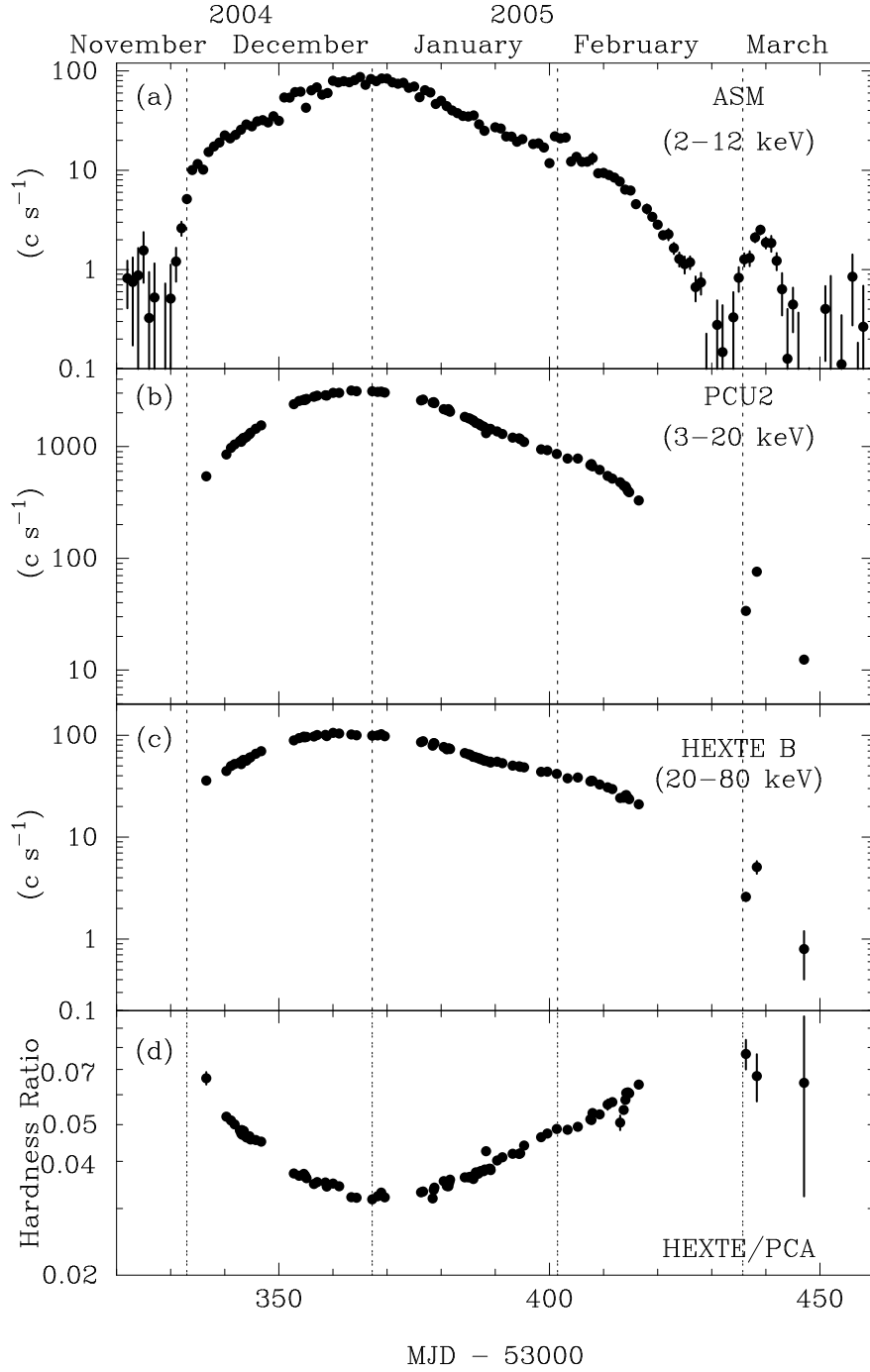


Fig. 1.— Background-subtracted count rates and hardness ratios of X0331+53 obtained from the *RXTE* observations. Dashed lines indicate the days of periastron passage (Zhang et al. 2005, and references therein). (a) The 2 – 10 keV ASM lightcurve, with 1 day binning. (b) The 3 – 20 keV PCU2 lightcurve. (c) The 20 – 80 keV HEXTE cluster B lightcurve. (d) The hardness ratio, defined as the ratio between the HEXTE and PCU count rates.

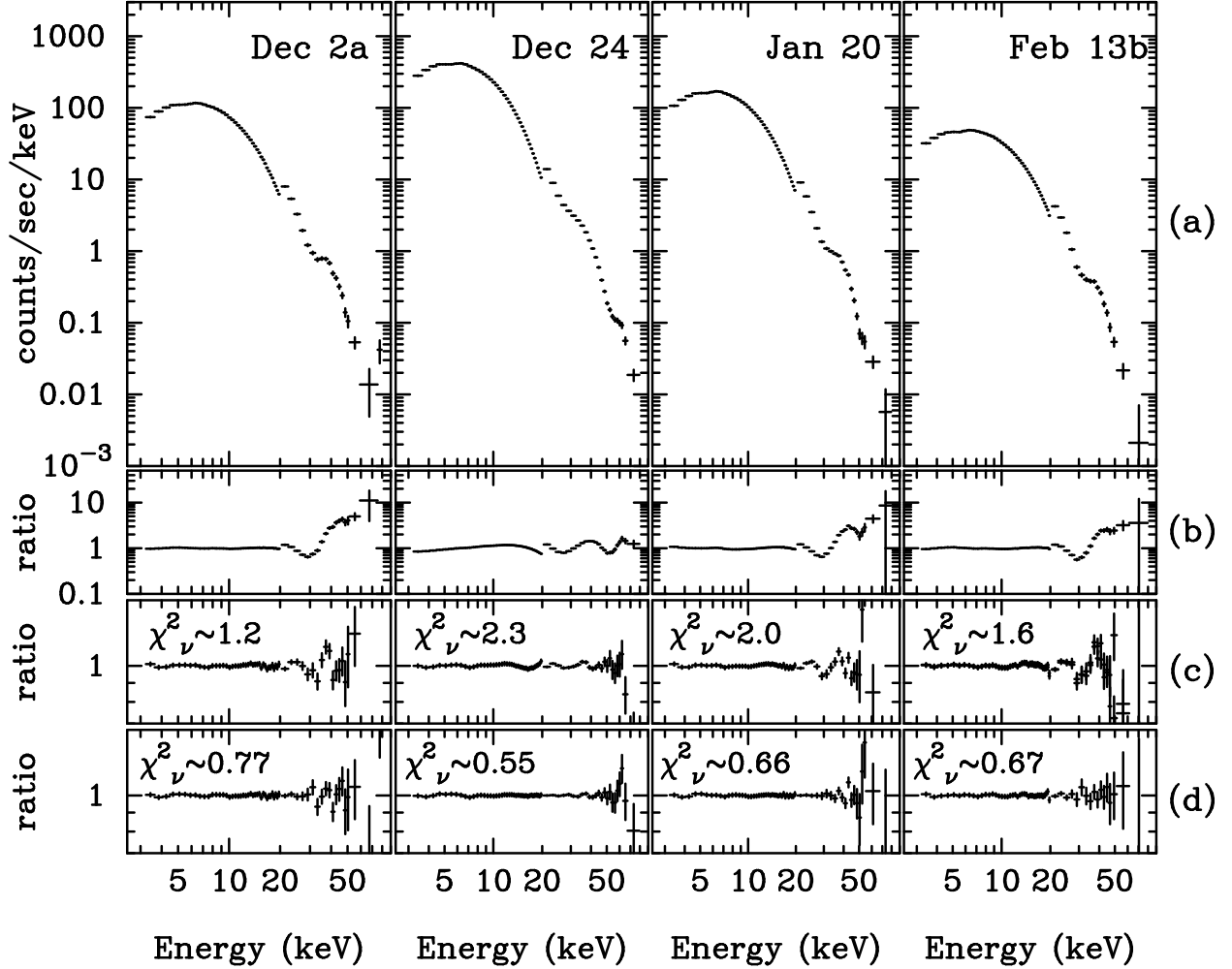


Fig. 2.— Representative pulse-phase-averaged spectra of X0331+53, obtained on Dec 2a, Dec 24, Jan 20, and Feb 13b. (a) The background-subtracted and response-inclusive PCA (3–20 keV) and HEXTE (20–80 keV) spectra. (b) The PCA and HEXTE spectra in panel (a), normalized to the best-fit NPEX models which incorporates no absorption factors. (c) The data to NPEX×CYAB2 model ratios. (d) The data to NPEX×CYAB2×GABS model ratios. Detailed model parameters are given in Table 2.

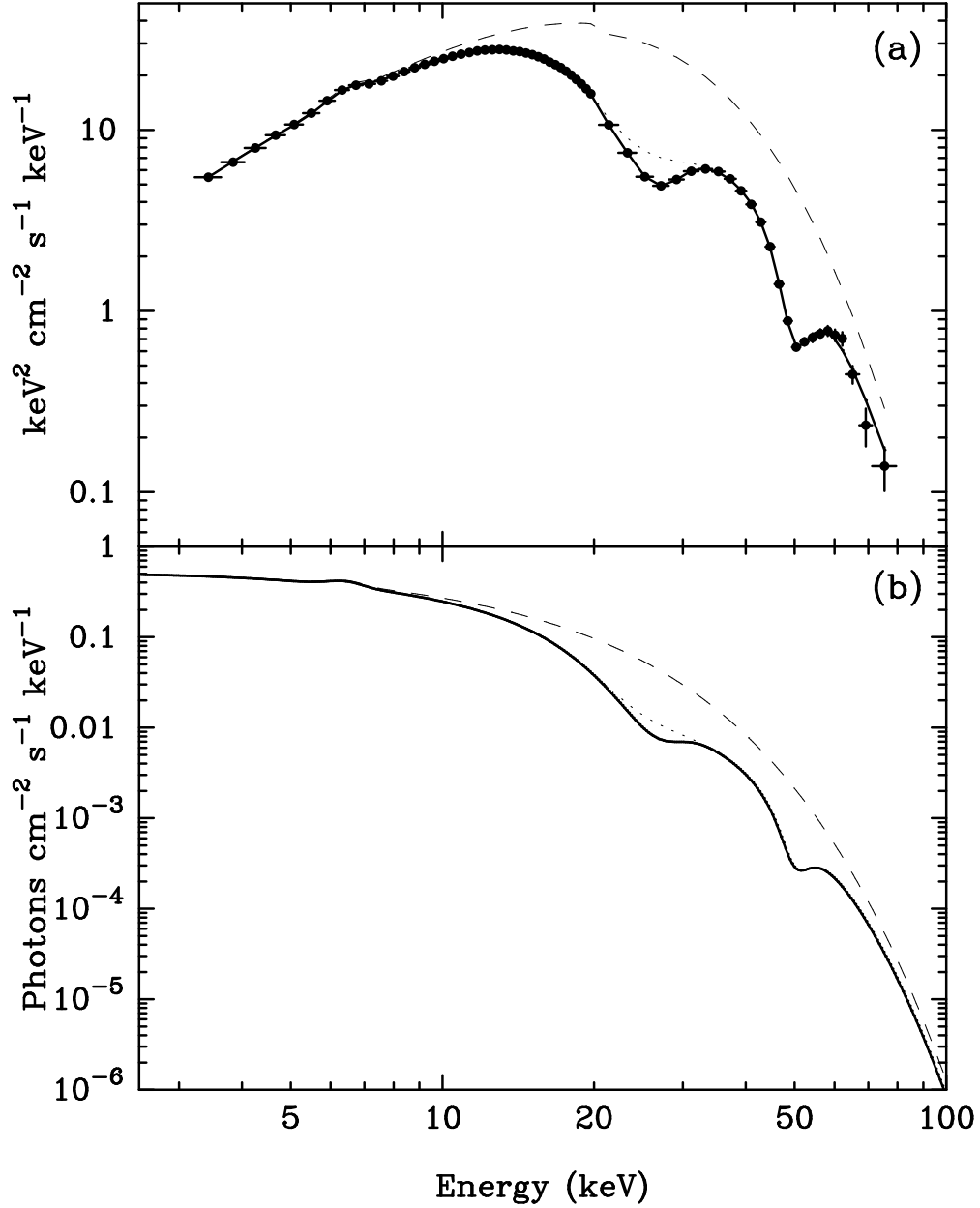


Fig. 3.— (a) The same Dec 24 spectrum as shown in Figure 2a, but presented in the deconvolved νF_ν form. The filled circles represent the data, and the solid lines are the best-fit NPEX×CYAB2×GABS model. The dotted curve represent the best-fit model, from which the GABS absorption factor is removed. The dashed lines display the NPEX continuum, obtained by further resetting the CYAB2 factor to zero. (b) The best-fit model in its incident form. Meanings of the solid, dotted, and dashed curves are the same as in panel a.

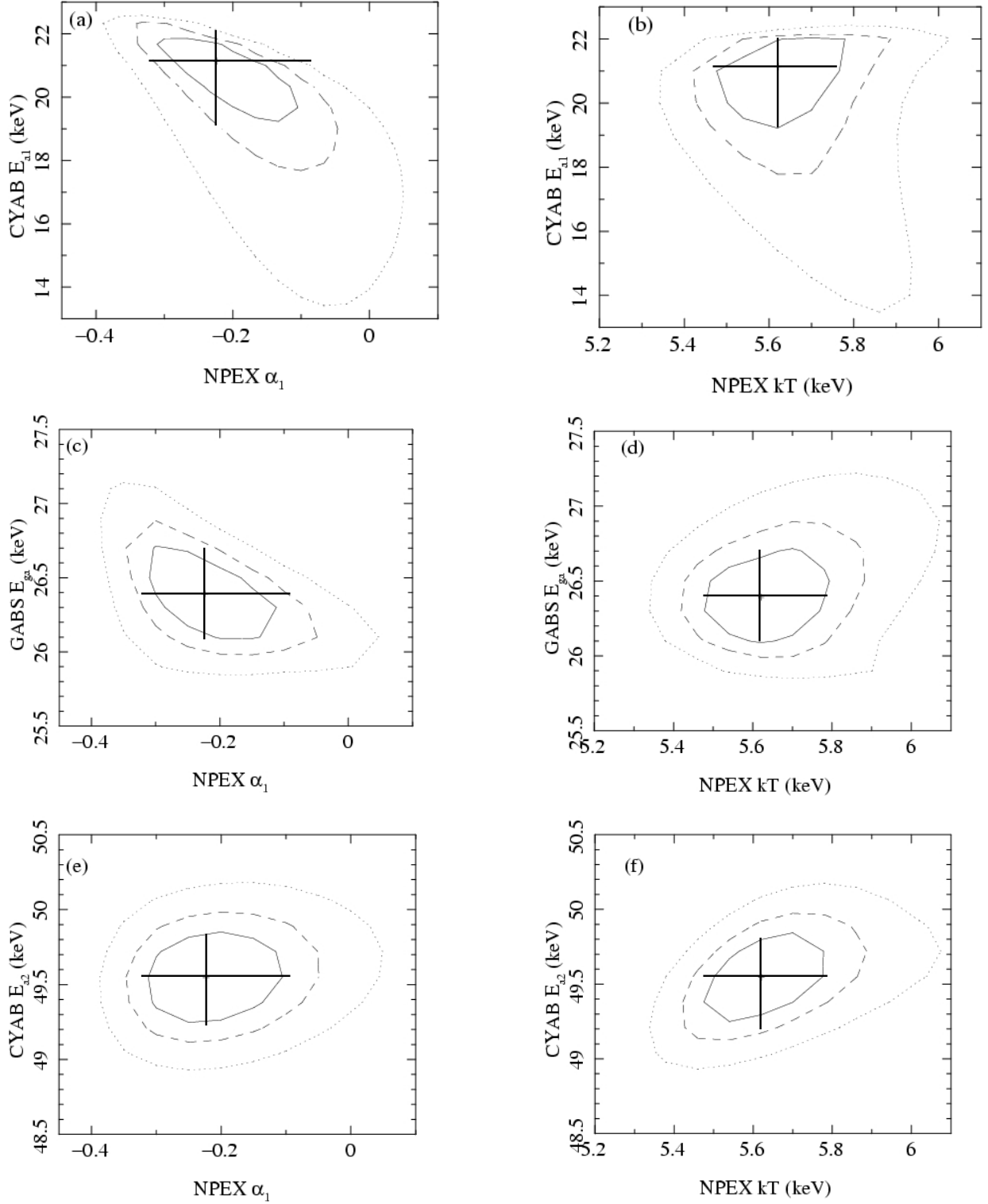


Fig. 4.— Confidence contours between the continuum and the CRSF parameters, obtained from spectral fitting to the Dec 24 data. The solid, dashed, and dotted lines represent 68%, 90%, and 99% confidence levels respectively. The crosses indicate 90%-confidence error ranges of the individual parameters given in Table 2.

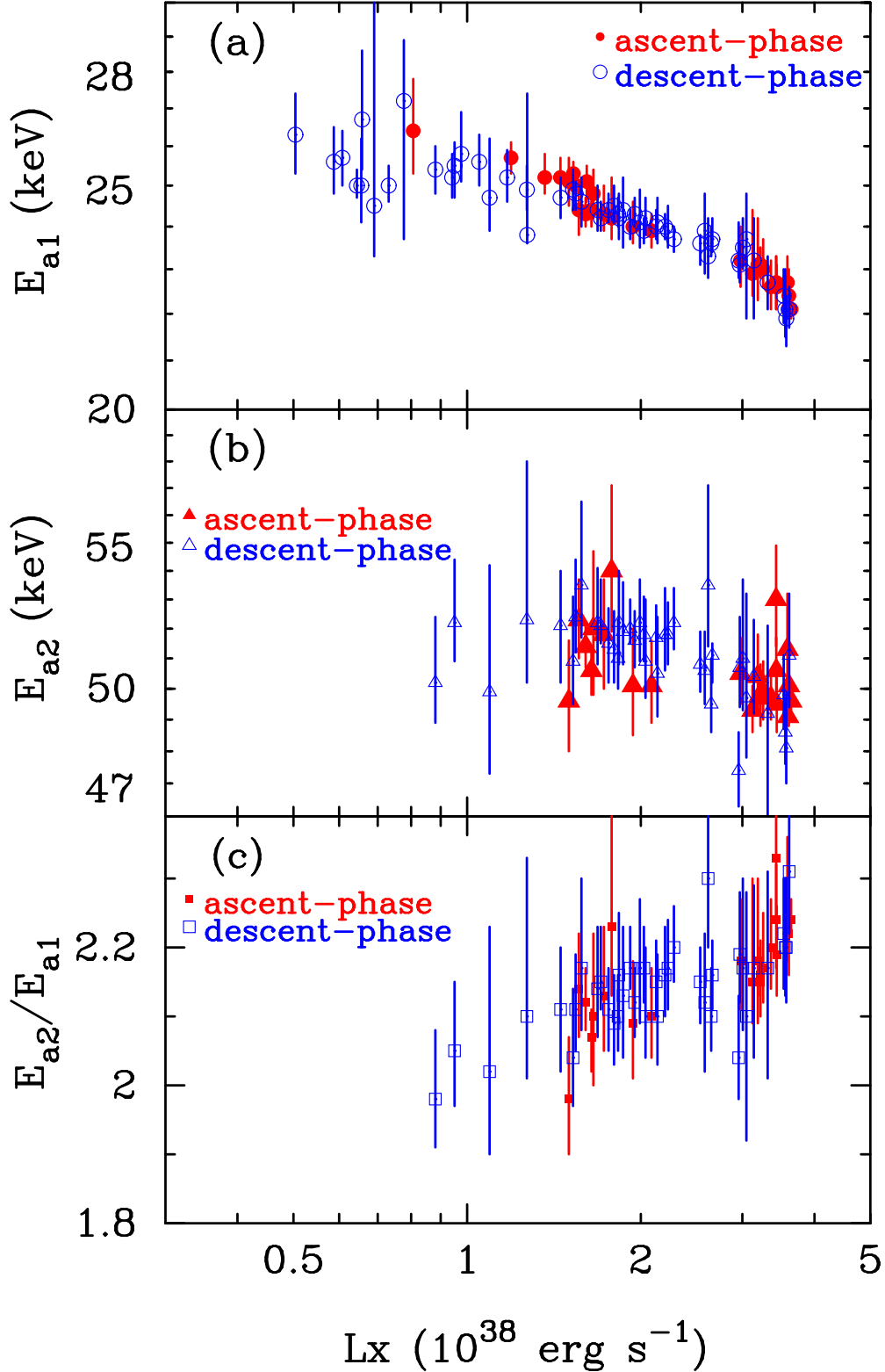


Fig. 5.— The fundamental (panel a) and second harmonic (panel b) cyclotron resonance energies, shown against the 3 – 80 keV luminosity. Panel (c) shows the ratios between panels (b) and (a). The plotted data are extracted from the daily-averaged data using the NPEX×CYAB2×GABS model fitting. The error bars represent 90% confidence levels. Those data in which E_{a2} is fixed at $2E_{a1}$ are omitted. The red and blue data represent the

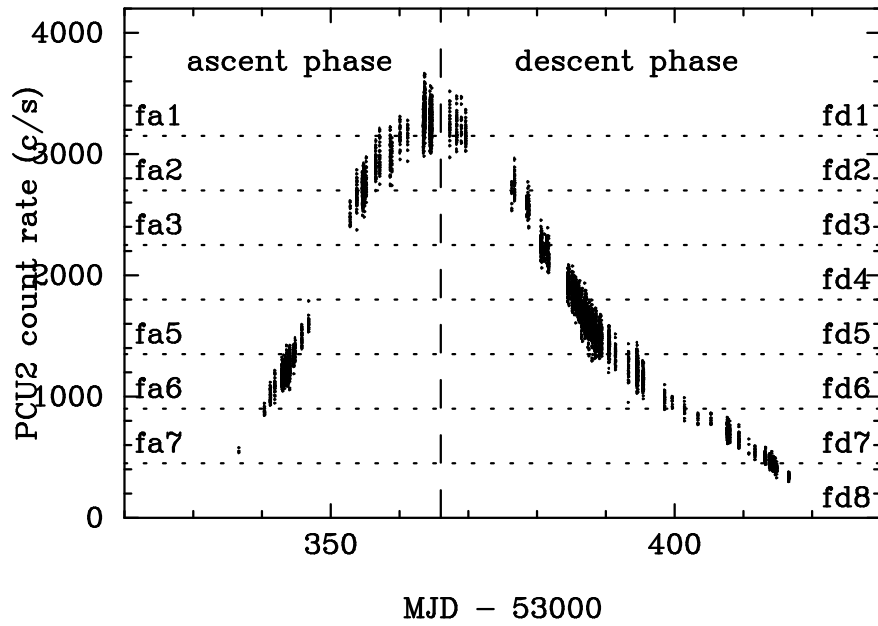


Fig. 6.— The whole PCU 2 lightcurve of X0331+53, plotted with 64 sec binnings. The horizontal dot lines represents boundaries of the flux sorting. The vertical dashed line divides the ascent and descent phases of the outburst.

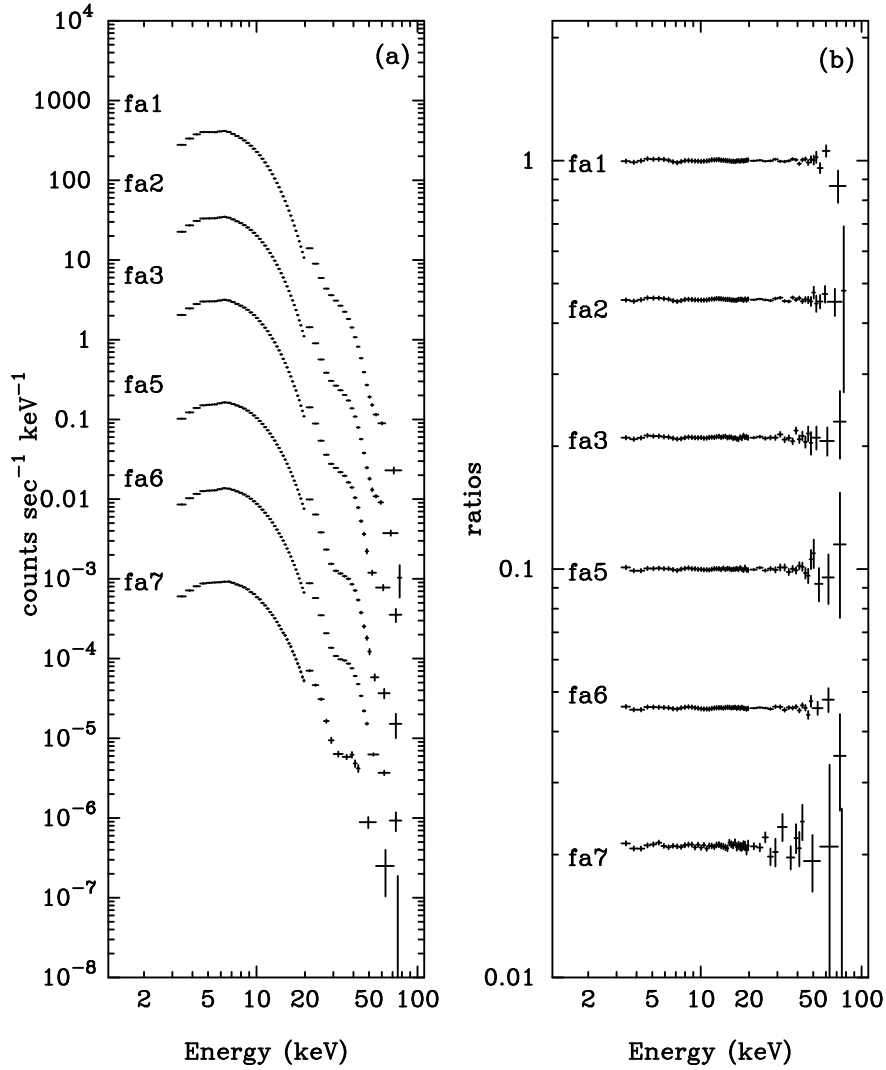


Fig. 7.— (a) Flux-sorted spectra of X0331+53 derived from the ascent phase. For clarity, they are shifted vertically by a factor of 0.5 between neighboring flux levels. (b) The spectra normalized to the best-fit NPEX×CYAB2×GABS model. The data are shifted vertically, in the same way as in panel (a).

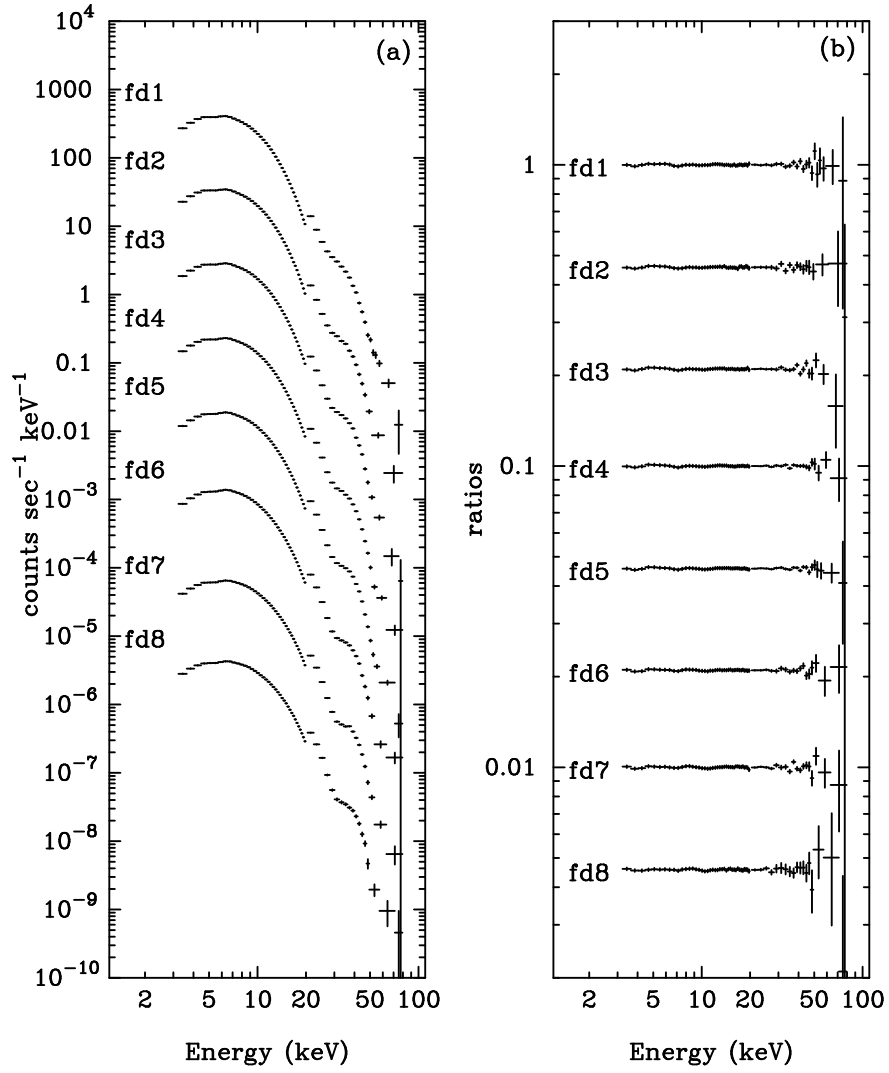


Fig. 8.— (a) Same as Figure 7, but the data are derived from the outburst descent phase.

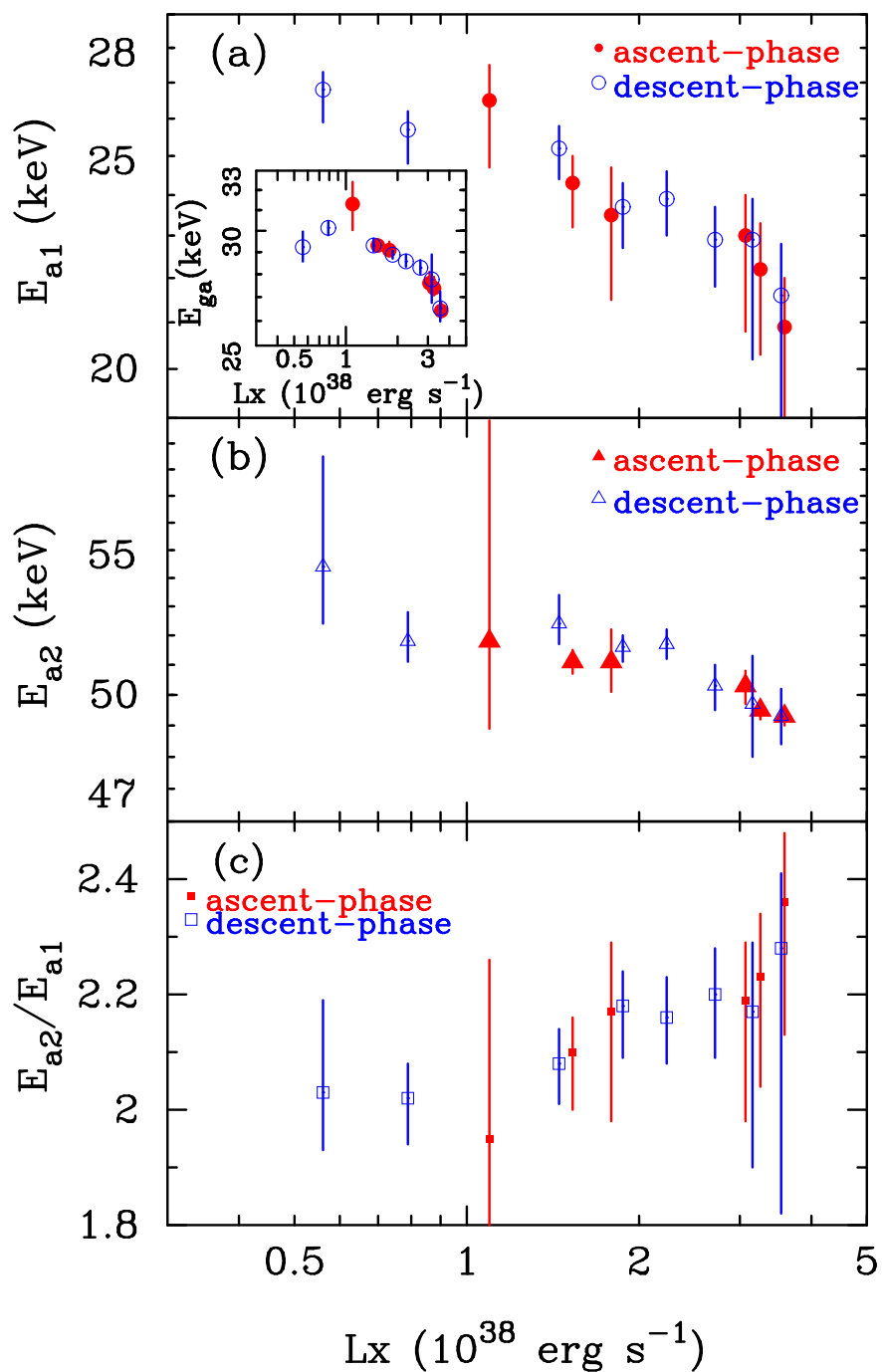


Fig. 9.— Same as Figure 5, but the results are derived using the flux-sorted spectra. The inset panel in (a) describes the luminosity dependence of the E_{ga} parameter.

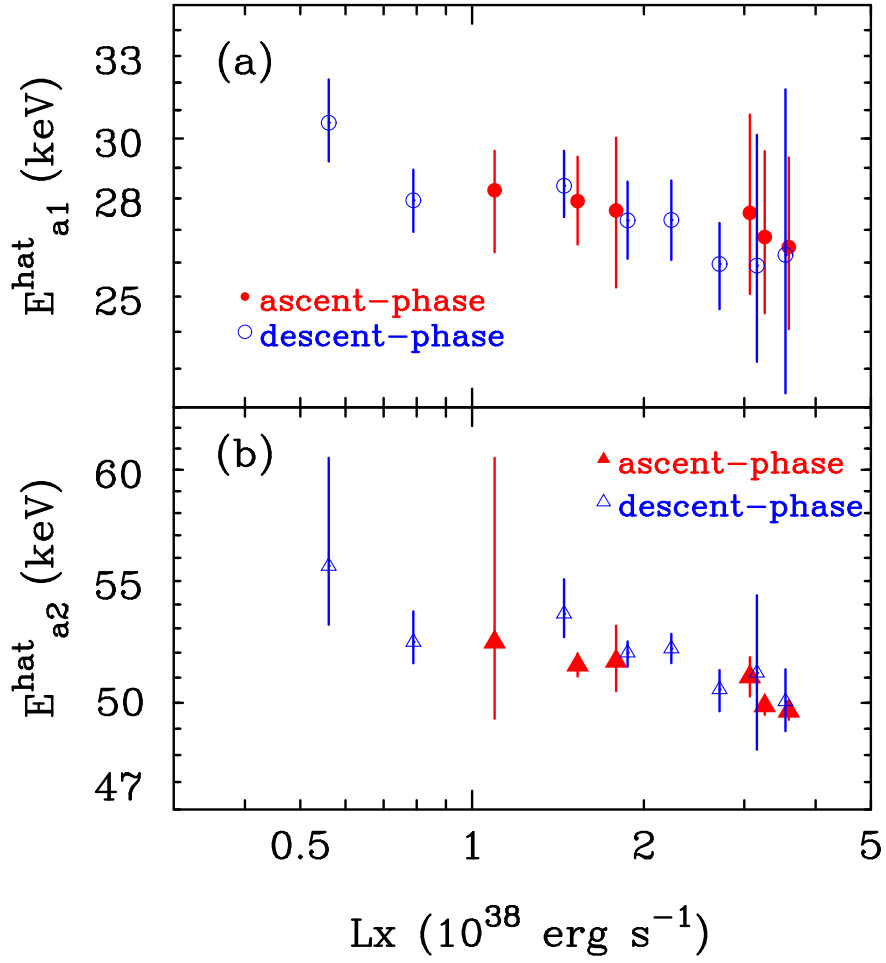


Fig. 10.— The luminosity dependence of \hat{E}_{a1} and \hat{E}_{a2} .

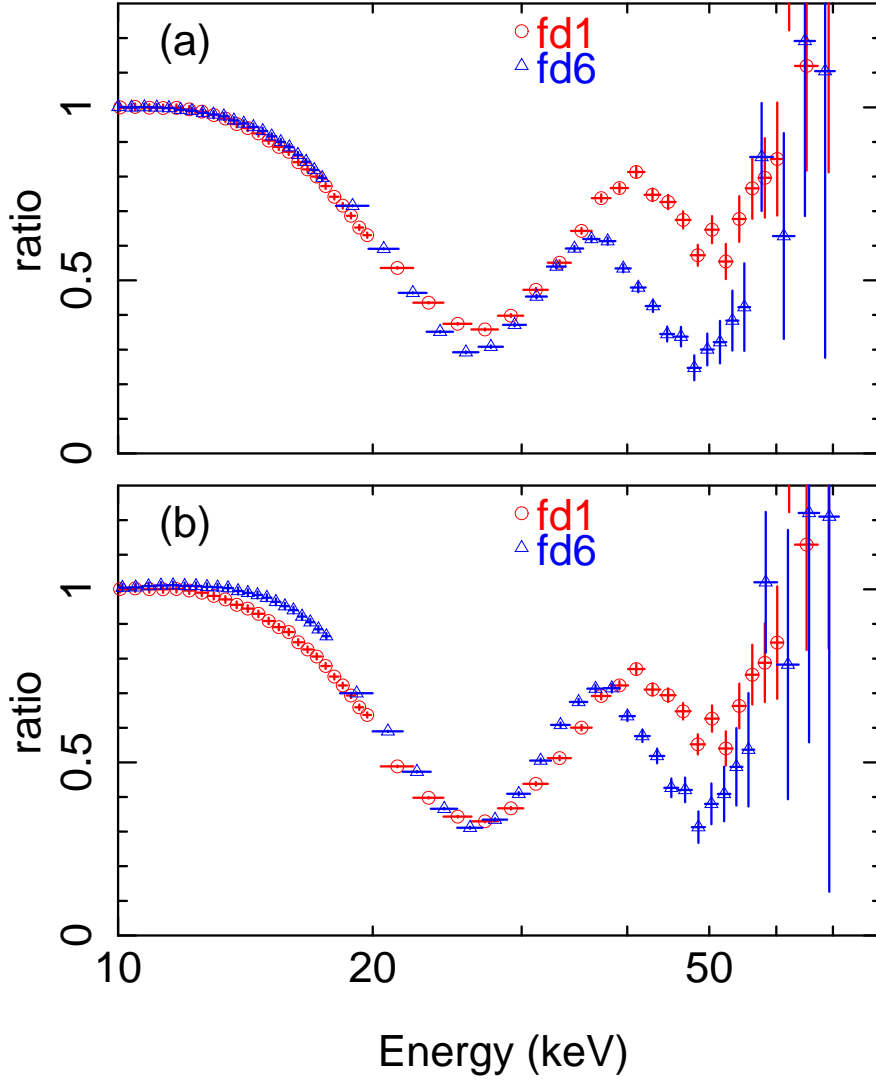


Fig. 11.— (a) The flux-sorted fd1 (red circles) and fd6 (blue triangles) spectra, normalized to the best-fit NPEX continuum determined individually using the 3–13 and 60–80 keV ranges only. The energy scale of the blue spectrum is scaled by a factor of 0.885, and it is compressed in the vertical direction by a factor of $1+(1-y)\times 0.38$ (with the ratio 1.0 kept as a pivot). The < 20 and > 20 keV ranges are covered by the PCA and HEXTE data, respectively. (b) The same as panel (a), but the PLCUT model is used as the continuum instead of NPEX. Again, the two continua are normalized to separate models. With respect to the red data points, the blue ones are scaled by a factor of 0.895 in the energy axis, and $1+(1-y)\times 0.40$ in the vertical direction.

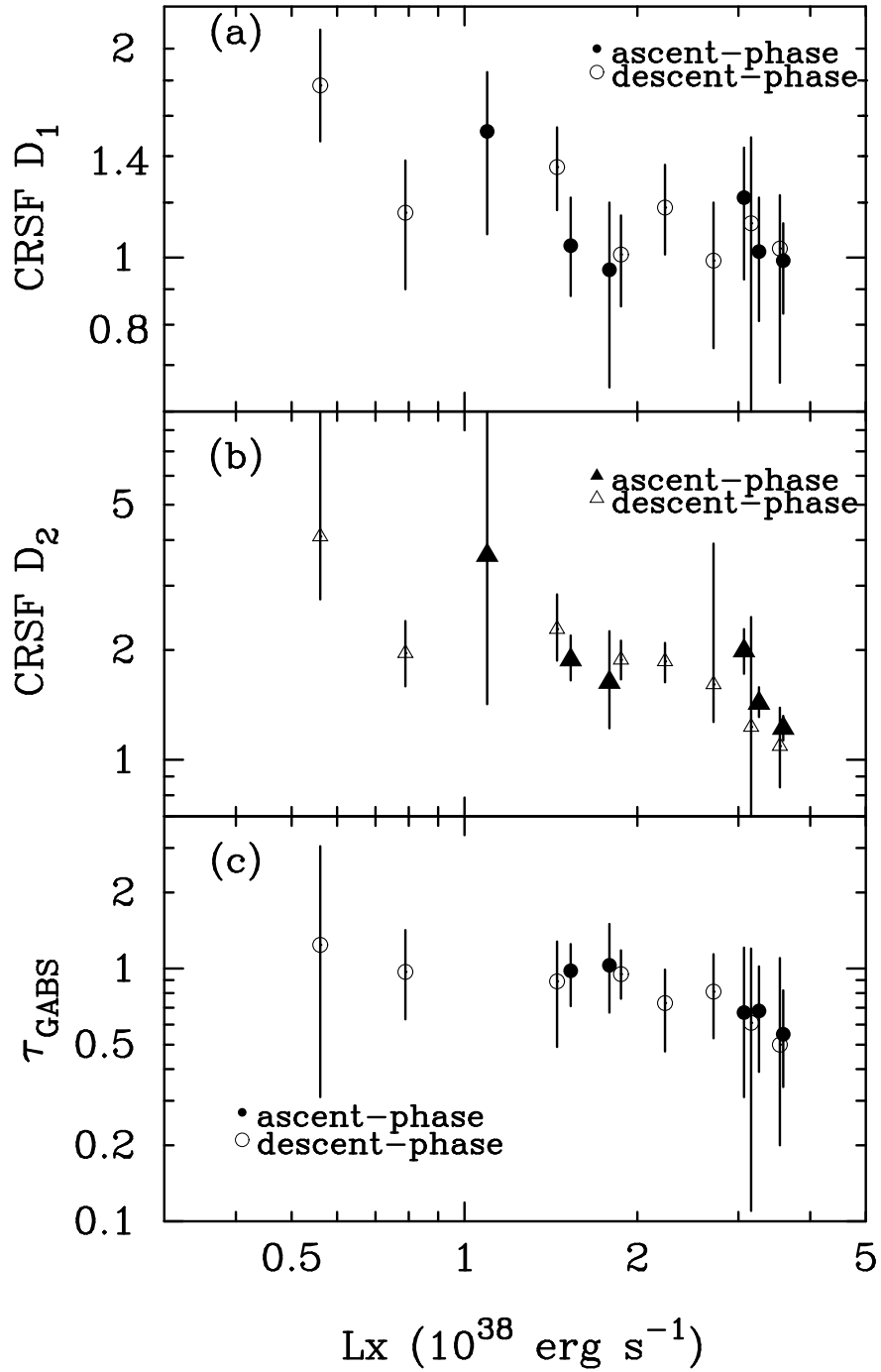


Fig. 12.— The CRSF depths derived from the flux-sorted spectra, plotted against the 3–80 keV source luminosity.

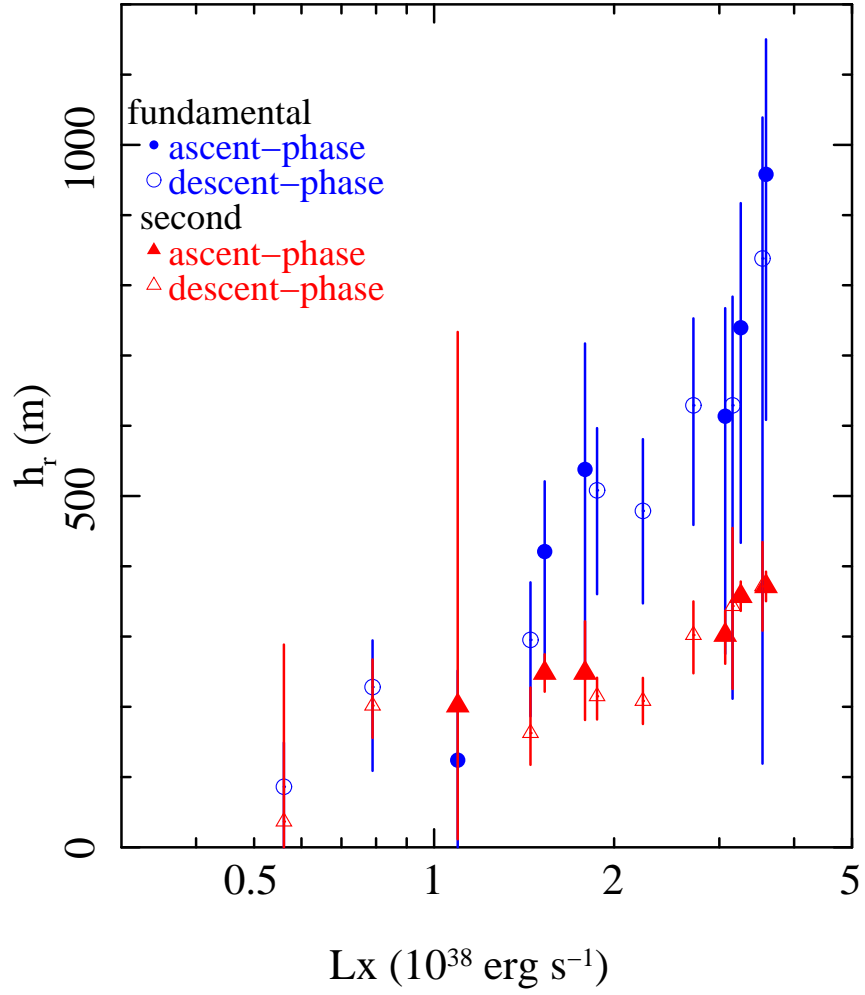


Fig. 13.— The estimated height of the CRSF forming regions against the 3 – 80 keV luminosity.

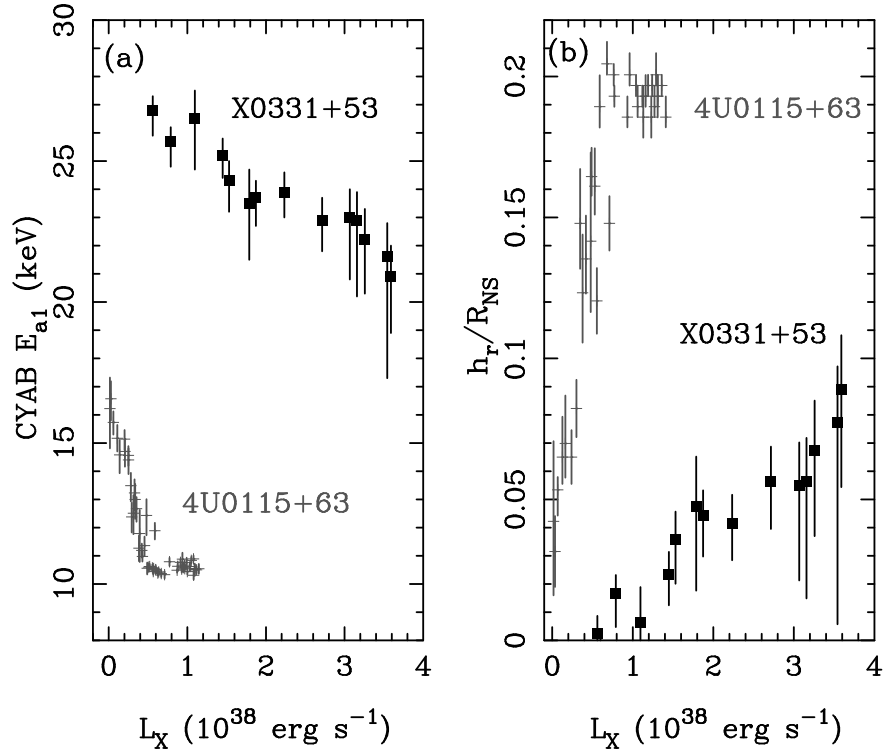


Fig. 14.— Comparison between X0331+53 and 4U 0115+63, in terms of the luminosity dependence of the fundamental resonance energy (panel a) and of the estimated cyclotron “photosphere” height. The CRSF are modeled with eq.2. The results of 4U 0115+63 refer to Nakajima et al. (2006a).

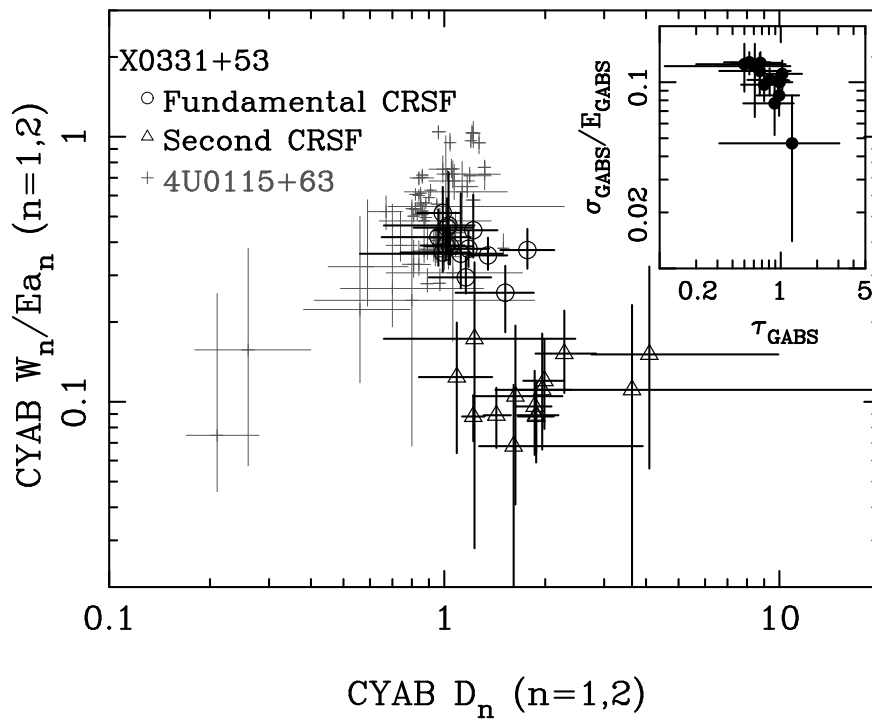


Fig. 15.— CRSF depths D of X0331+53, plotted against the fractional width W/E_a . Results on 4U 0115+63 (Nakajima et al. 2006a) are also shown for comparison.